J. Mech. Phys. Solids 216 (2026) 106769

Contents lists available at ScienceDirect

Journal of the Mechanics and Physics of Solids

journal homepage: www.elsevier.com/locate/jmps

Eulerian finite-deformation extension of Gurtin's distortion gradient plasticity: Formulation, $H(\mathrm{curl})$ finite element implementation, and applications

Andrea Panteghini [a], Lorenzo Bardella [a,*], M.B. Rubin [b]

[a] Department of Civil, Environmental, Architectural Engineering and Mathematics, Università degli Studi di Brescia, Italy

[b] Faculty of Mechanical Engineering, Technion-Israel Institute of Technology, Haifa, 32000, Israel

ARTICLE INFO

Keywords:
Small-scale metal plasticity
Strengthening and mechanisms
Nye-Kröner tensor
Finite deformation
Eulerian formulation
$H(\mathrm{curl})$ finite element

ABSTRACT

This work proposes an Eulerian finite-deformation formulation for phenomenological higher-order distortion gradient plasticity (DGP) as a basis to model the size-dependent behavior of metals when geometrically necessary dislocations (GNDs) play a role. Here, the adjective phenomenological refers to disregarding the crystal lattice and DGP recalls that the theory constitutively prescribes the plastic spin. The developed DGP extends to finite deformations the pivotal theory of Gurtin (2004, "A gradient theory of small-deformation isotropic plasticity that accounts for the Burgers vector and for dissipation due to plastic spin" J. Mech. Phys. Solids 52, 2545–2568), which relies on the Nye-Kröner dislocation density tensor. In this work, the extension of such a tensor to finite deformations is denoted as the Nye-Kröner-like tensor, $\boldsymbol{\alpha}$, to emphasize the alternatives discussed in the literature for its definition. The main pillars of the proposed Eulerian theory are two evolution equations: one for $\boldsymbol{\alpha}$ and one for the elastic distortional deformation tensor. The source term in the evolution equation for $\boldsymbol{\alpha}$ is the curl, operating in the current configuration, of the plastic rate tensor, which, for isochoric plastic flow, is a deviatoric non-symmetric tensor. Also, this evolution equation extends that based on the Jaumann rate by linearly combining the total spin rate and the plastic spin rate; such a combination is governed by a model parameter whose effect is assessed by resorting to numerical results. The evolution equation for the elastic distortional deformation tensor is discussed on the basis of different choices for the second-order tensor governing the contribution due to the rate of plasticity. This choice is important because it has an impact both on the mechanical response and on the complexity of the numerical time-integration. Additionally, the results of the theory are discussed in the light of two different constitutive choices for the nonlinear measure of the deviatoric elastic strain, one of them being Hencky's logarithmic strain. The higher-order contribution in the free-energy density is simply assumed to be quadratic in $\boldsymbol{\alpha}$, which is adequate for the purposes of this investigation, aiming to present the essential features of the proposed finite-deformation framework; in future studies, more sophisticated models will be combined with the theory here developed to predict actual size effects caused by GNDs. The exclusive use of $\boldsymbol{\alpha}$ as a higher-order primal field requires an $H(\mathrm{curl})$ finite element (FE) formulation, which is consistent with the weakest continuity requirements on the plastic rate tensor. A fully implicit FE algorithm is provided for plane strain. Its performance and results are evaluated on the basis of two large-deformation benchmark problems: the shearing of a strip under monotonic and cyclic loadings, allowing verification against

* Corresponding author.
E-mail addresses: andrea.panteghini@unibs.it (A. Panteghini), lorenzo.bardella@ing.unibs.it (L. Bardella), mbrubin@tx.technion.ac.il (M.B. Rubin).

https://doi.org/10.1016/j.jmps.2026.106769
Received 6 March 2026; Received in revised form 8 July 2026; Accepted 9 July 2026
Available online 10 July 2026

analytical estimates, and the necking of a plate, highlighting the role of the internal length in controlling strain localization and in governing size-dependent response. Overall, it is established that the proposed evolution equation for $\boldsymbol{\alpha}$ yields results that are free from spurious oscillations. When rotations are important in the boundary value problem at hand, the obtained results suggest that the spin rate governing the evolution equation for $\boldsymbol{\alpha}$ should be the elastic spin rate. For small elastic deformations, which is typical of metals, the predicted mechanical response is essentially insensitive to the adopted nonlinear elastic strain measure, so that computational efficiency may guide this choice. The necking problem shows that the notion of size dependence should compare the material length ℓ to the size of the region in which strain gradients are distributed (e.g. localized regions) and not to structural dimensions.

1. Introduction

This work proposes an Eulerian finite-deformation formulation for phenomenological higher-order strain gradient plasticity (SGP), which is intended to be a possible basis for the modeling of the size-dependent behavior of metals when geometrically necessary dislocations (GNDs, Ashby (1970)) play a role. Here, the adjective phenomenological refers to disregarding the crystal lattice.

The main feature of the adopted Eulerian framework is the mandatory use in the constitutive equations of quantities that are defined in the current configuration (Rubin, 2021). The developed SGP extends to finite deformations the pivotal theory of Gurtin (2004), which relies on the dislocation density tensor developed by Nye (1953) and Kröner (1962) in the framework of small strains and rotations. The extension to finite deformations of the Nye-Kröner tensor includes different possibilities, which have been long discussed in the literature (see, e.g., Cermelli and Gurtin (2001), and Arora et al. (2020), among several contributions). For this reason, in this paper, the terminology "Nye-Kröner-*like* tensor" is introduced to indicate any possible finite-deformation extension of the classical dislocation density tensor.

The small-deformation SGP of Gurtin (2004) is actually denoted as a distortion gradient plasticity (DGP, Bardella and Panteghini (2015)) to emphasize that it constitutively prescribes the plastic spin. Specifically, it defines a higher-order stress dependent on gradients of the plastic spin and a dissipative stress dependent on the plastic spin rate.

Because of the phenomenological nature of the theory considered, the definition of Nye-Kröner-like tensor developed here can more precisely be associated with the concept of incompatibility of inelastic deformation rates (see, e.g., Fosdick and Royer-Carfagni (2020), and references therein), rather than with the measure of a *net* Burgers vector. Rubin and Bardella (2024) discuss Eulerian rates of elastic incompatibilities relying on

$$-\mathrm{curl}\,\mathbf{L}_p\,, \tag{1}$$

where the curl operates in the current configuration and $\mathbf{L}_p$ is the plastic rate tensor, which is assumed to be traceless in this investigation and, in theories relying on the multiplicative decomposition of the deformation gradient $\mathbf{F}$ (Bilby et al., 1957; Kröner, 1959; Lee, 1969), corresponds to $\mathbf{F}_e\dot{\mathbf{F}}_p\mathbf{F}_p^{-1}\mathbf{F}_e^{-1}$, with $\mathbf{F}_e$ and $\mathbf{F}_p$ denoting the elastic and plastic parts of $\mathbf{F}=\mathbf{F}_e\mathbf{F}_p$ and $\dot{()}$ denoting material time differentiation. The second-order tensor in Eq. (1) measures the evolution of elastic incompatibility. In Rubin and Bardella (2024), this incompatibility is studied in phenomenological Eulerian finite-deformation elastoplasticity. One of the results in Rubin and Bardella (2024) concerns the importance of the plastic spin rate tensor, defined as

$$\mathbf{W}_p=\frac{1}{2}(\mathbf{L}_p-\mathbf{L}_p^T)\,,$$

in determining the incompatibility. Additionally, the Eulerian rates of elastic incompatibilities developed on the basis of (1) have been used in Rubin and Bardella (2024) to propose a size-dependent hardening characterizing a lower-order DGP theory.

A more effective way to develop a SGP theory is to resort to a higher-order framework, which allows the specification of higher-order boundary conditions, for instance imposing that densities of dislocations either can exit the body or pile-up at the boundary, thus triggering gradients of plastic flow. To achieve this within an Eulerian formulation of the constitutive equations, one has to define an evolution equation to time-integrate $\mathrm{curl}\,\mathbf{L}_p$, with the purpose of obtaining a total Nye-Kröner-like tensor, here denoted with the symbol $\boldsymbol{\alpha}$. This tensor, then, is the higher-order primal field entering the contribution to the Helmholtz free-energy density referred to as the defect energy by Gurtin (2004). Differentiating the defect energy with respect to $\boldsymbol{\alpha}$ gives the defect stress entering the higher-order balance.

Hence, in Gurtin's formulation the plastic spin is a primal kinematic variable. Although its importance in predicting size effects is well-established for small strains (see, e.g., Bardella (2009), Bardella and Panteghini (2015), Poh and Peerlings (2016), and references therein), here it is emphasized that its introduction as a primal field becomes even more crucial at finite deformations. In particular, within an Eulerian setting, where the evolution of elastic distortion depends on the difference between the velocity gradient $\mathbf{L}$ and the plastic rate tensor $\mathbf{L}_p$, this theoretical framework ensures a fully consistent specification of $\mathbf{L}_p$.

An evolution equation for $\boldsymbol{\alpha}$ has been proposed in Rubin and Bardella (2023) within the context of a higher-order DGP encompassing two distinct plasticity fields, a higher-order one and a conventional one, which has been shown to be able to accurately predict the yield stress scaling (Panteghini et al., 2025a). The present work limits attention to an Eulerian finite-deformation extension of the pioneering DGP proposed by Gurtin (2004), such that it involves only one (higher-order) plasticity field. Here, the evolution equation for the Eulerian Nye-Kröner-like tensor is proposed in the form

$$\dot{\boldsymbol{\alpha}}=\boldsymbol{\Omega}\boldsymbol{\alpha}+\boldsymbol{\alpha}\boldsymbol{\Omega}^T+\mathrm{curl}\,\mathbf{L}_p\,, \tag{2}$$

where the second-order skew-symmetric tensor $\boldsymbol{\Omega}$ is defined as

$$\boldsymbol{\Omega} = \mathbf{W} - k_\Omega \, \mathbf{W}_p \, , \tag{3}$$

in which

$$\mathbf{W} = \frac{1}{2}(\mathbf{L} - \mathbf{L}^T)$$

is the spin rate and k_Ω is a material parameter that controls the objective rate of $\boldsymbol{\alpha}$. Eq. (2) is actually more general than that proposed in Rubin and Bardella (2023) if restricted to a single plasticity field, this one being recovered for $k_\Omega = 0$, that is the Jaumann rate. Since the former contribution of Steinmann (1996), other formulations of the Nye-Kröner-like tensor rely, to the best of the authors' knowledge, on the multiplicative decomposition of the deformation gradient into elastic and plastic parts, $\mathbf{F} = \mathbf{F}_e\mathbf{F}_p$, which is not admissible in the Eulerian formulation of the constitutive equations followed here because of the presence of the intermediate configuration (Rubin, 2012). Most of these formulations are discussed by Cermelli and Gurtin (2001). Among them, Willis (1967) proposed to determine the Nye-Kröner-like tensor by applying the curl in the current configuration to $\mathbf{F}_e^{-1}$, which has been later followed to develop the mesoscale field dislocation mechanics (MFDM) theory (Acharya and Zhang, 2015). It is worth mentioning a few differences concerned with different definitions of the Nye-Kröner-like tensor. For instance, $\mathrm{curl}\mathbf{F}_e^{-1}$ is a two-point tensor, while $\boldsymbol{\alpha}$ in Eq. (2) is a second-order tensor in the current configuration, as required by the adopted Eulerian framework. Additionally, in the $\mathbf{F} = \mathbf{F}_e\mathbf{F}_p$ framework, even if a physical equivalence between some definitions of the Nye-Kröner-like tensor can be established by the relations between different configurations in which Stokes' theorem is applied to evaluate the net Burgers vector, if one then adopts the same mathematical form of the defect energy (e.g., quadratic) for Nye-Kröner-like tensors defined in different configurations, different material responses are obtained, not only quantitatively, but also qualitatively (as shown by Abatour et al. (2023), for a finite-deformation SGP in which the higher-order stress is a vector dependent on the gradient of a scalar micromorphic field related to the cumulative plastic strain).

Although the present investigation deals with phenomenological plasticity, here the literature on crystal plasticity is briefly discussed because of its importance in small-scale metal plasticity with particular reference to the Nye-Kröner-like dislocation density tensor. Actually, the present finite-deformation theory could be combined with crystal plasticity through the micromorphic approach of Forest and co-workers (Cordero et al., 2010), so that the present phenomenological model can be used for finite-deformation strain gradient crystal plasticity without facing the complexity of imposing higher-order boundary conditions in crystal plasticity relying on the Nye-Kröner-like tensor (Gurtin and Needleman, 2005). In the context of crystal plasticity, Gurtin (2006) has shown that the Nye-Kröner-like tensor proposed by Cermelli and Gurtin (2001) has a plastically convected rate that depends only on pure densities of geometrically necessary dislocations (GNDs, Ashby (1970)), as in its original small-strain version (Fleck and Hutchinson, 1997; Arsenlis and Parks, 1999). To the best of the authors' knowledge, this is a common feature of all $\mathbf{F}_e\mathbf{F}_p$-based formulations for the Nye-Kröner-like tensor in the literature, where the crystallographic directions are held constant as defined in the intermediate or initial configurations. In contrast, Bardella et al. (2025) have shown that the Eulerian form $\mathrm{curl}\,\mathbf{L}_p$ naturally accounts also for the incompatibility due to the elastic distortion of the crystal lattice, because the curl is applied not only to the plastic slip rates, but also to the crystallographic directions, which are vector fields dependent on the lattice distortion, as formerly discussed by Asaro and Rice (1977) for conventional (i.e. size-independent) crystal plasticity. Noticeably, Bardella et al. (2025) have also shown that the contribution to incompatibility due to the lattice distortion may be as important as that due to densities of GNDs.

The formulation of the proposed theory is developed, in Section 2, such that the Eulerian constitutive equation for the Cauchy stress can have different forms, depending on the adopted distortional nonlinear elastic strain measure, in general denoted with the symbol $\boldsymbol{\mathcal{E}}'_e$. This investigation focuses on two possibilities for $\boldsymbol{\mathcal{E}}'_e$, namely, half of either the deviatoric part or the logarithm of the unimodular elastic left Cauchy-Green tensor. The first choice has the computational advantage of avoiding the spectral decomposition of the elastic strain tensor, thus making the implementation easier and more efficient in finite-deformation elastoplasticity (Panteghini, 2024; Panteghini et al., 2025b). However, discussing the possibility of different choices for $\boldsymbol{\mathcal{E}}'_e$ is interesting, both to better understand the theoretical framework and to establish whether the known properties of the logarithmic strain (see, e.g., Latorre and Montáns (2014)) are needed in small-scale metal plasticity.

A more general evolution equation for the distortional elastic left-Cauchy-Green tensor than that used in Rubin and Bardella (2023) was proposed in Rubin (1994) and is used here. The merits of this evolution equation are twofold. First, it ensures consistency between the elastic rate tensor and the difference between the velocity gradient and the plastic rate tensor. Second, the recoverable second-order stress tensor entering the higher-order balance equation, and coupling it with the conventional linear momentum balance, results to be always coincident with the deviatoric part of the Cauchy stress tensor, independent of the adopted $\boldsymbol{\mathcal{E}}'_e$.

Given that this work aims to demonstrate the essential features of the proposed Eulerian finite-deformation framework, the defect energy is simply assumed to be quadratic in $\boldsymbol{\alpha}$. Since this form of the defect energy is known to be inadequate to describe actual size effects exhibited by metals that are caused by GND densities (Groma et al., 2003, 2007; Forest and Guéninchault, 2013; Mesarovic et al., 2015; Bardella and Panteghini, 2015; Panteghini et al., 2019), in future studies, more sophisticated models will be combined with the finite-deformation theory here presented to predict the actual size effects, as detailed among the open issues of the Concluding Remarks (Section 5).

The finite element (FE) formulation developed in this work extends that presented in Panteghini and Bardella (2018), thus implementing, for the first time to the best of the authors' knowledge, $H(\mathrm{curl})$ FEs for finite deformations. These FEs are needed to ensure the correct continuity requirements for $\mathbf{L}_p$, and then to correctly apply the higher-order boundary conditions, resulting from the use of the Nye-Kröner-like tensor as exclusive primal higher-order kinematic field. Details of a fully implicit FE algorithm for plane-strain problems are illustrated in Section 3 and the related user element subroutine (uel) for the FE code Abaqus/Simulia (Dassault Systèmes, 2024) is provided in the supplementary material.

In briefly discussing the literature on higher-order finite-deformation theories using Nye-Kröner-like tensors, here only investigations that do not disregard the plastic spin rate are considered, i.e. only DGP theories. Kaiser and Menzel (2019) propose a finite-deformation DGP, relying on the multiplicative decomposition of the deformation gradient, where the Nye-Kröner-like tensor is defined as $\mathrm{Curl}\,\mathbf{F}_p$, where the Curl operates in the reference configuration, and the defect energy is, as here, quadratic in the Nye-Kröner-like tensor. Kaiser and Menzel (2019) show that their theory can regularize certain deformation modes even in the presence of softening. However, this is aided by the FE adopted in Kaiser and Menzel (2019), in which all the components of the higher-order fields are nodal degrees of freedom, thus overconstraining them with respect to the precise requirement of the Curl operator (Wieners and Wohlmuth, 2011). In fact, even within small strains and rotations and for perfect plasticity, allowing $\mathbf{L}_p$ to jump as permitted by the curl operator leads to non-uniqueness of the solution for the plastic field in several benchmarks (Bittencourt et al., 2003; Bardella and Giacomini, 2008; Poh and Peerlings, 2016; Panteghini and Bardella, 2018). It is inferred that the predictions of the correct $H(\mathrm{curl})$ FE implementation and of the FE implementation in which all components of $\mathbf{L}_p$ are nodal degrees of freedom will exhibit even larger discrepancies in the finite-deformation regime.

Still within the $\mathbf{F}_e\mathbf{F}_p$ framework, in Aslan et al. (2011) Forest and co-workers present a micromorphic DGP theory where the higher-order kinematic field is the Curl of a second-order "microdeformation" tensor, that requires the same continuity conditions as $\mathbf{L}_p$ in this work and is related to a plastic rate tensor obtained from crystal plasticity through a penalty addition to the free-energy density. Moreover, in the framework of crystal plasticity, both the IMDEA-Madrid group of Llorca and Segurado and the Los Alamos National Laboratory group of Capolungo and Lebensohn propose implementations based on the fast Fourier transform to obtain solutions of DGP problems relying on Nye-Kröner-like tensors. Specifically, for such a tensor, Haouala et al. (2020) adopt $\mathrm{Curl}\,\mathbf{F}_p$, as in Kaiser and Menzel (2019), while Zecevic et al. (2023) use the formulation of Cermelli and Gurtin (2001), that is $\mathbf{F}_p\,\mathrm{Curl}\,\mathbf{F}_p$. Finally, Arora et al. (2020) present a FE implementation of Acharya's finite-deformation MFDM theory, which, even if it is outside the realm of higher-order SGP, relies on $\mathrm{curl}\mathbf{F}_e^{-1}$ for the Nye-Kröner-like tensor, it noticeably disregards $\mathbf{F}_p$, and it describes GND-based plasticity in much greater detail than the phenomenological theory concerned with in this investigation; the MFDM, in fact, includes also a conservation law for the evolution of the net Burgers vector and a dislocation velocity field, which make the solution of boundary value problems much more challenging and the FE formulation very different from that developed here.

The theory proposed here is discussed, in Section 4, on the basis of numerical results obtained for the cyclic shearing of an unbounded strip and for the necking of a bar under tension. Cyclic shearing allows unveiling specific features of the proposed theory and verifying the FE implementation by comparison with analytical estimates, thanks to the adopted quadratic defect energy. The necking problem is characterized by softening in the force-displacement response and allows assessment of the influence of the material length on strain localization and structural size effects. Additionally, the necking problem modeled by the proposed DGP is interesting because it features higher-order effects even for very large bar size, due to the coupling between large deformations and localization of plastic flow gradients.

Delving into some details of the obtained results, changing the value of k_Ω in the evolution equation (2)-(3) for $\boldsymbol{\alpha}$ has negligible effect on the necking problem, while it affects some aspects of the solution for the cyclic shearing, where rotations are more important. The obtained results show that $k_\Omega = 1$, making $\boldsymbol{\Omega}$ coincident with the elastic spin rate, leads to finite-deformation results closer to the predictions under the assumption of small strains and rotations. For all the considered values of k_Ω, however, the proposed evolution equation for $\boldsymbol{\alpha}$ yields results that are free from spurious oscillations.

Regarding the constitutive choice for $\mathcal{E}'_e$, it is shown that, for material parameters typical of metals, implying small elastic deformation, it has a negligible influence on the mechanical response, possibly because of the adopted pressure-independent plasticity (Panteghini et al., 2025b). This suggests that $\mathcal{E}'_e$ should be chosen on the basis of computational efficiency.

2. Eulerian finite-deformation distortion gradient plasticity relying on the Nye-Kröner dislocation density tensor

The theory presented in this section extends to finite deformations that of Gurtin (2004) by modifying the theory proposed in Rubin and Bardella (2023), and by specializing it to the case of a single plasticity field. Moreover, the theory is developed in such a way as to leave the freedom of selecting different measures for the deviatoric nonlinear elastic strain $\mathcal{E}'_e$. For this constitutive choice, two possibilities are considered in detail in this investigation: first, the one in Rubin and Bardella (2023), where $\mathcal{E}'_e$ is half of the deviatoric part of the elastic distortional left Cauchy-Green tensor $\bar{\mathbf{B}}_e$, where the overline denotes a unimodular tensor (i.e. $\det\bar{\mathbf{B}}_e = 1$); second, $\mathcal{E}'_e$ is assumed to be $(\ln\bar{\mathbf{B}}_e)/2$, i.e. the deviatoric logarithmic strain (Hencky, 1933).

2.1. Kinematics

In the theory developed in Rubin and Bardella (2023), which builds on the formulation of Rubin and Attia (1996), the evolution equation for the elastic distortional deformation tensor $\bar{\mathbf{B}}_e$ is proposed in the form

$$\dot{\bar{\mathbf{B}}}_e = \mathbf{L}'\bar{\mathbf{B}}_e + \bar{\mathbf{B}}_e\mathbf{L}'^T - \mathbf{A}\,, \tag{4}$$

where $()'$ denotes the deviatoric part of a second-order tensor, $\mathbf{A}$ is a second-order tensor accounting for the rate of plasticity, and the velocity gradient is defined as

$$\mathbf{L} = \mathrm{grad}\,\dot{\mathbf{x}}\,,$$

where $\mathbf{x}$ is the current position of a material point and grad operates in the current configuration.

For the reasons introduced in Section 1 and explained in the following, this investigation uses a form of $\mathbf{A}$ different from that proposed in Rubin and Bardella (2023) for their size-dependent plastic rate field. Specifically, by following the Eulerian formulation of constitutive equations for the evolution equations of microstructural vectors in Rubin (1994), $\mathbf{A}$ is defined as

$$\mathbf{A} = \mathbf{L}_p \bar{\mathbf{B}}_e + \bar{\mathbf{B}}_e \mathbf{L}_p^T , \quad \text{with} \quad \mathrm{tr}(\mathbf{L}_p) = 0 , \tag{5}$$

such that Eq. (4) becomes

$$\dot{\bar{\mathbf{B}}}_e = (\mathbf{L}' - \mathbf{L}_p)\bar{\mathbf{B}}_e + \bar{\mathbf{B}}_e(\mathbf{L}' - \mathbf{L}_p)^T = \mathbf{L}'_e \bar{\mathbf{B}}_e + \bar{\mathbf{B}}_e \mathbf{L}'^T_e , \tag{6}$$

where $\mathbf{L}'_e = \mathbf{L}' - \mathbf{L}_p$ can be interpreted as the deviatoric part of the elastic rate tensor. The unimodularity of $\bar{\mathbf{B}}_e$ is ensured in Eq. (6) by verifying that $\dot{\bar{\mathbf{B}}}_e \cdot \bar{\mathbf{B}}_e^{-1} = 0$. Here and henceforth, $\mathbf{B} \cdot \mathbf{C} = \mathrm{tr}(\mathbf{B}\mathbf{C}^T)$ denotes the inner product of two second-order tensors $\mathbf{B}$ and $\mathbf{C}$. An evolution equation alternative to Eq. (6), which uses for $\mathbf{A}$ the proposal in Rubin and Bardella (2023) for the size-dependent plastic rate field, is discussed in Appendix A.

From Eq. (6), it follows that the deviatoric part $\bar{\mathbf{B}}'_e$ of $\bar{\mathbf{B}}_e$ satisfies the evolution equation

$$\dot{\bar{\mathbf{B}}}'_e = \mathbf{L}'\bar{\mathbf{B}}_e + \bar{\mathbf{B}}_e \mathbf{L}'^T - \frac{2}{3}(\mathbf{D}' \cdot \bar{\mathbf{B}}_e)\mathbf{I} - \mathbf{A}', \quad \mathbf{A}' = \mathbf{L}_p \bar{\mathbf{B}}_e + \bar{\mathbf{B}}_e \mathbf{L}_p^T - \frac{2}{3}(\mathbf{D}_p \cdot \bar{\mathbf{B}}_e)\mathbf{I} , \tag{7}$$

where

$$\mathbf{D} = \frac{1}{2}(\mathbf{L} + \mathbf{L}^T)$$

is the total deformation rate, $\mathbf{I}$ is the second-order identity tensor, and

$$\mathbf{D}_p = \frac{1}{2}(\mathbf{L}_p + \mathbf{L}_p^T)$$

is the plastic deformation rate.

Given $\bar{\mathbf{B}}'_e$, $\bar{\mathbf{B}}_e$ is determined by imposing the unimodular condition for $\bar{\mathbf{B}}_e$, i.e.

$$\det\left(\frac{\beta_1}{3}\mathbf{I} + \bar{\mathbf{B}}'_e\right) = 1 \quad \text{with} \quad \beta_1 = \mathrm{tr}(\bar{\mathbf{B}}_e) , \tag{8}$$

which gives the third-order scalar equation

$$\beta_1^3 - \frac{9}{2}\left(\bar{\mathbf{B}}'_e \cdot \bar{\mathbf{B}}'_e\right)\beta_1 + 27\left(\det \bar{\mathbf{B}}'_e - 1\right) = 0 \tag{9}$$

to be solved for β_1. Following Lagioia et al. (2014), the correct solution of Eq. (9) is always the largest solution for β_1, which is equal to

$$\beta_1 = \begin{cases} 3 \quad \text{if} \quad \bar{\mathbf{B}}'_e \cdot \bar{\mathbf{B}}'_e = 0 \\ \sqrt{6\left(\bar{\mathbf{B}}'_e \cdot \bar{\mathbf{B}}'_e\right)} \cos\left[\frac{1}{3}\arccos\left(-3\sqrt{6}\frac{(\det \bar{\mathbf{B}}'_e - 1)}{\sqrt{(\bar{\mathbf{B}}'_e \cdot \bar{\mathbf{B}}'_e)^3}}\right)\right] \quad \text{if} \quad \left(\bar{\mathbf{B}}'_e \cdot \bar{\mathbf{B}}'_e\right)^3 \geq 54\left(\det \bar{\mathbf{B}}'_e - 1\right)^2 \\ \sqrt{6\left(\bar{\mathbf{B}}'_e \cdot \bar{\mathbf{B}}'_e\right)} \cosh\left[\frac{1}{3}\mathrm{arccosh}\left(-3\sqrt{6}\frac{(\det \bar{\mathbf{B}}'_e - 1)}{\sqrt{(\bar{\mathbf{B}}'_e \cdot \bar{\mathbf{B}}'_e)^3}}\right)\right] \quad \text{if} \quad \left(\bar{\mathbf{B}}'_e \cdot \bar{\mathbf{B}}'_e\right)^3 < 54\left(\det \bar{\mathbf{B}}'_e - 1\right)^2 \end{cases} \tag{10}$$

It is assumed that the volumetric response is purely elastic, so the elastic dilatation J_e coincides with the total dilatation J, that is

$$J_e = J = \det \mathbf{F} , \tag{11}$$

where

$$\mathbf{F} = \mathrm{Grad}\, \mathbf{x} ,$$

with Grad operating in the reference configuration. Hence, the volume ratio satisfies the evolution equation

$$\frac{\dot{J}}{J} = \mathrm{tr}(\mathbf{D}) . \tag{12}$$

Of course, the set of kinematic equations includes the fundamental relations introduced in Section 1.

2.2. Balance laws and higher-order boundary conditions

The conventional linear momentum balance, in the absence of body forces and inertia, reads

$$\mathrm{div}\, \mathbf{T} = \mathbf{0} , \tag{13}$$

where $\mathbf{T}$ is the Cauchy stress and the divergence operates in the current configuration. Of course, the balance law (13) is subject to the usual conventional boundary conditions.

The higher-order balance correlates three second-order stress tensors in the law (Gurtin, 2004; Rubin and Bardella, 2023)

$$(\mathrm{curl}\, \boldsymbol{\zeta})' + \mathbf{S} - \mathbf{M} = \mathbf{0} , \tag{14}$$

where $\boldsymbol{\zeta}$ is the recoverable higher-order stress dependent on the Nye-Kröner-like tensor $\boldsymbol{\alpha}$, usually referred to as the defect stress (Gurtin, 2004), $\mathbf{S}$ is a dissipative stress dependent on the plastic rate tensor $\mathbf{L}_p$, and $\mathbf{M}$ is a recoverable stress that depends on elasticity and couples the balance Eqs. (13) and (14). Because of the form of $\mathbf{A}$ in Eq. (5) adopted in this investigation, $\mathbf{M}$ coincides with the deviatoric part of the Cauchy stress, as shown in the following. This may not be the case for forms of $\mathbf{A}$ different from that in Eq. (5), as with the proposal for the size-dependent plasticity field in Rubin and Bardella (2023), which is discussed in Appendix A. Note, however, that any acceptable form of $\mathbf{A}$ must yield an $\mathbf{M}$ stress that specializes to $\mathbf{T}'$ under small strains and rotations to recover the theory of Gurtin (2004).

The balance law in Eq. (14) requires higher-order boundary conditions. By splitting the boundary ∂P into the two *complementary* subsets ∂P_k and ∂P_s, the so-called "microhard" condition is specified as Gurtin (2004)

$$\mathbf{L}_p \times \mathbf{n} = \mathbf{0} \quad \text{on} \quad \partial P_k\,, \tag{15}$$

which ensures that (densities of) dislocations do not penetrate the boundary ∂P_k, thus implying that dislocations pile up on ∂P_k and contribute to GNDs (Ashby, 1970; Fleck and Hutchinson, 1997; Gurtin, 2004). The dual "microfree" condition requires

$$\boldsymbol{\zeta} \times \mathbf{n} = \mathbf{0} \quad \text{on} \quad \partial P_s\,, \tag{16}$$

which states that dislocations are free to exit the body P through the boundary ∂P_s. Obviously, it would be possible to specify non-homogeneous higher-order boundary conditions, but they are not considered in this investigation.

Notation. Consider a fixed orthonormal Cartesian triad $\mathbf{e}_i$, a second-order tensor $\mathbf{G}$, and a vector $\mathbf{n}$. Then, in this investigation, $\operatorname{curl}\mathbf{G}$ and $\mathbf{G}\times\mathbf{n}$ are defined such that $(\operatorname{curl}\mathbf{G})\cdot(\mathbf{e}_i\otimes\mathbf{e}_j) \equiv \epsilon_{jkl}\partial \mathrm{G}_{il}/\partial x_k$ and $(\mathbf{G}\times\mathbf{n})\cdot(\mathbf{e}_i\otimes\mathbf{e}_j) \equiv \epsilon_{jlk}G_{il}n_k$, respectively, where $\otimes$ indicates the tensor product, $\epsilon_{ijk} = (i-j)(j-k)(k-i)/2$ is the Levi-Civita (alternating) tensor, $G_{ij} = \mathbf{G}\cdot(\mathbf{e}_i\otimes\mathbf{e}_j)$, $x_i = \mathbf{x}\cdot\mathbf{e}_i$, $n_i = \mathbf{n}\cdot\mathbf{e}_i$, and the summation convention is adopted over repeated indices.

2.3. The constitutive equations

The definition of the stresses is guided by the rate of material dissipation, which, in the isothermal case, reads (Rubin and Bardella, 2023)

$$\rho\theta\xi' = -p\,\mathrm{tr}(\mathbf{D}) + \mathbf{T}'\cdot\mathbf{D}' - \rho\dot{\psi} + \mathbf{S}\cdot\mathbf{L}_p - \mathbf{M}\cdot\mathbf{D}_p + \boldsymbol{\zeta}\cdot\operatorname{curl}\mathbf{L}_p \geq 0 \quad \text{with} \quad \mathbf{T}' = \mathbf{T} + p\mathbf{I}\,, \tag{17}$$

where ρ is the current mass density, θ is the constant absolute temperature, ξ' is the specific internal rate of production of entropy due to material dissipation,

$$p = -\frac{1}{3}\mathrm{tr}(\mathbf{T}) \tag{18}$$

is the pressure (positive under compression), and ψ is the Helmholtz free-energy density.

It is assumed that the free energy admits the additive decomposition

$$\rho_z\psi = \Psi^{\mathrm{v}}_{\mathrm{el}}(J) + \Psi'_{\mathrm{el}}(\gamma_1) + \Psi_{\mathrm{d}}(\boldsymbol{\alpha})\,, \tag{19}$$

where $\rho_z = J\rho$ denotes the material zero-stress density, $\Psi^{\mathrm{v}}_{\mathrm{el}}(J)$ is the contribution to $\rho_z\psi$ due to the elastic dilatation, $\Psi'_{\mathrm{el}}(\gamma_1)$ accounts for the elastic distortion, thus being a function of the invariant γ_1 of the deviatoric elastic strain $\boldsymbol{\mathcal{E}}'_e$, with both γ_1 and $\boldsymbol{\mathcal{E}}'_e$ still to be selected, and $\Psi_{\mathrm{d}}(\boldsymbol{\alpha})$ is the so-called defect energy (Gurtin, 2004).

By substituting the general form of the free energy in Eq. (19) into Eq. (17) and using Eq. (12), one obtains

$$\rho\theta\xi' = -\big(p + \frac{\mathrm{d}\Psi^{\mathrm{v}}_{\mathrm{el}}}{\mathrm{d}J}\big)\mathrm{tr}(\mathbf{D}) + \mathbf{T}'\cdot\mathbf{D}' + \mathbf{S}\cdot\mathbf{L}_p - \mathbf{M}\cdot\mathbf{D}_p - \frac{\rho}{\rho_z}\frac{\mathrm{d}\Psi'_{\mathrm{el}}}{\mathrm{d}\gamma_1}\dot{\gamma}_1 + \big(\boldsymbol{\zeta} - \frac{\rho}{\rho_z}\frac{\mathrm{d}\Psi_{\mathrm{d}}}{\mathrm{d}\boldsymbol{\alpha}}\big)\cdot(\operatorname{curl}\mathbf{L}_p) \geq 0\,. \tag{20}$$

By selecting

$$\Psi^{\mathrm{v}}_{\mathrm{el}}(J) = k(1 - J + J\ln J)\,, \quad \Psi_{\mathrm{d}}(\boldsymbol{\alpha}) = \frac{1}{2}\mu\ell^2\boldsymbol{\alpha}\cdot\boldsymbol{\alpha}\,,$$

where k and μ are the bulk and shear moduli, respectively, and ℓ is a constant material length scale, Eq. (20) implies

$$p = -k\ln J\,, \quad \boldsymbol{\zeta} = \frac{1}{J}\mu\ell^2\boldsymbol{\alpha}\,, \tag{21}$$

thus reducing Eq. (20) to

$$\rho\theta\xi' = \mathbf{T}'\cdot\mathbf{D}' + \mathbf{S}\cdot\mathbf{L}_p - \mathbf{M}\cdot\mathbf{D}_p - \frac{\rho}{\rho_z}\frac{\partial\Psi'_{\mathrm{el}}}{\partial\gamma_1}\dot{\gamma}_1 \geq 0\,. \tag{22}$$

Note that this investigation considers the simplest possible form of $\Psi_{\mathrm{d}}(\boldsymbol{\alpha})$, but other forms are possible, for instance encompassing three invariants of $\boldsymbol{\alpha}$ and less-than-quadratic dependence on $\boldsymbol{\alpha}$. Although these extensions are important in order to model the size-dependent response of actual metals (see, e.g., Conti and Ortiz (2005), Ohno and Okumura (2007), Bardella (2010), Forest and Guéninchault (2013), Wulfinghoff et al. (2015), Bardella and Panteghini (2015), Panteghini et al. (2019), Panteghini and Bardella (2020), and references therein), this kind of study is beyond the scope of this investigation and left for future studies.

By following Gurtin (2004), the dissipative stress $\mathbf{S}$ dependent on $\mathbf{L}_p$ is prescribed as

$$\mathbf{S}_{\mathrm{D}} = \frac{2}{3} S V(d_p) \frac{\mathbf{D}_p}{d_p}\,, \quad \mathbf{S}_{\mathrm{W}} = \chi S V(d_p) \frac{\mathbf{W}_p}{d_p}\,,$$
$$d_p = \sqrt{\frac{2}{3}|\mathbf{D}_p|^2 + \chi |\mathbf{W}_p|^2} \geq 0\,, \quad SV(d_p) = \sqrt{\frac{3}{2}|\mathbf{S}_{\mathrm{D}}|^2 + \frac{1}{\chi}|\mathbf{S}_{\mathrm{W}}|^2} \geq 0\,, \tag{23}$$

where d_p is an effective plastic distortion rate, $|\mathbf{A}| \equiv \sqrt{\mathbf{A}\cdot\mathbf{A}}$ denotes the modulus of the tensor $\mathbf{A}$, $\mathbf{S}$ is separated into its symmetric, $\mathbf{S}_{\mathrm{D}} = (\mathbf{S}+\mathbf{S}^T)/2$, and skew-symmetric, $\mathbf{S}_{\mathrm{W}} = (\mathbf{S}-\mathbf{S}^T)/2$, parts, $\chi \geq 0$ is a parameter governing the dissipation associated with the plasticity spin rate,[1] and the product $SV(d_p)$ accounts for isotropic hardening and viscoplasticity as follows.

The effective stress S is constitutively prescribed as a function of the loading history through the isotropic hardening law

$$S = S(\bar{\varepsilon}_p)\,, \quad \bar{\varepsilon}_p = \int_0^t d_p \,\mathrm{d}t\,, \tag{24}$$

where $\bar{\varepsilon}_p$ denotes the accumulated effective plastic strain.

The viscoplastic function $V(d_p)$ is chosen as in Bardella and Panteghini (2015), Panteghini and Bardella (2016) in the form

$$V(d_p) = \begin{cases} \frac{d_p}{2\dot{\varepsilon}_0} & \text{if } \frac{d_p}{\dot{\varepsilon}_0} \leq 1 \\ 1 - \frac{1}{2}\frac{\dot{\varepsilon}_0}{d_p} & \text{if } \frac{d_p}{\dot{\varepsilon}_0} > 1 \end{cases} \tag{25}$$

with $\dot{\varepsilon}_0$ denoting a rate-sensitivity material parameter. For small values of $\dot{\varepsilon}_0$ the response is rate-independent except for the small region near the elastic-plastic transition. Note that the assumed isochoric plastic flow implies $\mathrm{tr}(\mathbf{L}_p) \equiv \mathrm{tr}(\mathbf{D}_p) = \mathrm{tr}(\mathbf{S}) = 0$.

Then, Eq. (22) is reduced to

$$\rho\theta\xi' = \mathbf{T}'\cdot\mathbf{D}' + SV(d_p)d_p - \mathbf{M}\cdot\mathbf{D}_p - \frac{\rho}{\rho_z}\frac{\partial \Psi'_{\mathrm{el}}}{\partial \gamma_1}\dot{\gamma}_1 \geq 0\,. \tag{26}$$

Now, a slightly more general form of the free energy ψ than that in Eq. (19) is considered to derive a result for the stress $\mathbf{M}$. For general elastically isotropic response, ψ can be expressed as

$$\psi = \psi(\mathcal{V})\,, \quad \mathcal{V} = \left\{ J, \bar{\mathbf{B}}_e, \boldsymbol{\alpha} \right\}.$$

Since ψ must be uninfluenced by superposed rigid body motions, ψ may depend on the tensors in $\mathcal{V}$ only through their invariants. In particular, this means that

$$\frac{\partial\psi}{\partial\bar{\mathbf{B}}_e}\bar{\mathbf{B}}_e = \bar{\mathbf{B}}_e\frac{\partial\psi}{\partial\bar{\mathbf{B}}_e}\,.$$

Consequently, by using Eq. (6),

$$\frac{\partial\psi}{\partial\bar{\mathbf{B}}_e}\cdot\dot{\bar{\mathbf{B}}}_e = 2\left(\frac{\partial\psi}{\partial\bar{\mathbf{B}}_e}\bar{\mathbf{B}}_e\right)\cdot(\mathbf{D}'-\mathbf{D}_p)\,.$$

Then, the rate of material dissipation in Eq. (26) can be rewritten as

$$\rho\theta\xi' = \mathbf{T}'\cdot\mathbf{D}' + SV(d_p)d_p - \mathbf{M}\cdot\mathbf{D}_p - 2\frac{\rho}{\rho_z}\left(\frac{\partial\psi}{\partial\bar{\mathbf{B}}_e}\bar{\mathbf{B}}_e\right)\cdot(\mathbf{D}'-\mathbf{D}_p)\,,$$

which, noticeably, indicates that

$$\mathbf{T}' = \mathbf{M} = \frac{2}{J}\left(\frac{\partial\psi}{\partial\bar{\mathbf{B}}_e}\bar{\mathbf{B}}_e\right)'\,, \tag{27}$$

regardless of the specific dependence of ψ on $\bar{\mathbf{B}}_e$. Specifically, this holds also in the special case here of interest with dependence of ψ on a single invariant of $\bar{\mathbf{B}}_e$ as specified in Eq. (19). Once the constitutive choice for Ψ'_{el} and γ_1 is made, the expression for $\mathbf{T}' = \mathbf{M}$ can be derived and, from Eq. (26), the dissipation inequality is satisfied, as it results

$$\rho\theta\xi' = SV(d_p)d_p > 0 \quad \forall \mathbf{L}_p \neq \mathbf{0}\,.$$

Back to the case in which the free-energy density depends on a single invariant of $\bar{\mathbf{B}}_e$, this investigation considers two possible constitutive choices for $\Psi'_{\mathrm{el}}(\gamma_1)$, as specified in the next two subsections.

[1] Note that $\chi = 0$ yields $\mathbf{S}_{\mathrm{W}} = \mathbf{0}$ and $\mathbf{W}_p$ free to develop, while irrotational plastic flow is obtained in the limit $\chi \to \infty$.

2.3.1. The B_e model

In this formulation, which is the one followed in Rubin and Bardella (2023),

$$\gamma_1 = \beta_1\,, \quad \Psi'_{\rm el} = \frac{1}{2}\mu(\beta_1 - 3)\,, \quad \mathcal{E}'_e = \frac{1}{2}\bar{\mathbf{B}}'_e\,, \tag{28}$$

such that, from Eqs. (6) and (8), one obtains

$$\dot{\beta}_1 = 2\bar{\mathbf{B}}'_e \cdot (\mathbf{D}' - \mathbf{D}_p)\,,$$

which, by using Eq. (26), leads to

$$\mathbf{T}' = \mathbf{M} = \frac{\mu}{J}\bar{\mathbf{B}}'_e\,. \tag{29}$$

2.3.2. The LN model

In this formulation,

$$\mathcal{E}'_e = \mathbf{E}'_e := \frac{1}{2}\ln\bar{\mathbf{B}}_e\,, \quad \gamma_1 = \mathbf{E}'_e \cdot \mathbf{E}'_e\,, \quad \Psi'_{\rm el} = \mu\gamma_1\,, \tag{30}$$

with $\mathbf{E}'_e$ denoting the distortional part of the logarithmic strain (Hencky, 1933), which is also a traceless tensor.

By using the formulæ obtained by Jog (2008), after some algebra, one has

$$\dot{\gamma}_1 = \frac{1}{2}(\ln\bar{\mathbf{B}}_e) \cdot \overline{\ln\bar{\mathbf{B}}_e}^{\,\cdot} = \frac{1}{2}\left(\sum_{i=1}^{3}\ln\bar{b}_{ei}\mathbf{P}_i\right) \cdot \left(\sum_{i=1}^{3}\frac{1}{\bar{b}_{ei}}\mathbf{P}_i\dot{\bar{\mathbf{B}}}_e\mathbf{P}_i\right) = \frac{1}{2}\sum_{i=1}^{3}\frac{\dot{\bar{b}}_{ei}}{\bar{b}_{ei}}\ln\bar{b}_{ei} = \mathrm{tr}(\mathbf{E}'_e\bar{\mathbf{B}}_e^{-1}\dot{\bar{\mathbf{B}}}_e) = \mathrm{tr}(\bar{\mathbf{B}}_e^{-1}\mathbf{E}'_e\dot{\bar{\mathbf{B}}}_e)\,, \tag{31}$$

in which $\bar{b}_{ei}$, with $i = 1,2,3$, are the eigenvalues of $\bar{\mathbf{B}}_e$ and the last equality is due to the fact that $\mathbf{E}'_e$ and $\bar{\mathbf{B}}_e^{-1}$ have the same principal directions $\mathbf{N}_i$, with $i = 1,2,3$ and $\mathbf{P}_i = \mathbf{N}_i \otimes \mathbf{N}_i$ (no sum on i). Note that the second equality in Eq. (31) is possible because the contributions due to the rotations of the eigenvectors entering $\overline{\ln\bar{\mathbf{B}}_e}^{\,\cdot}$ cancel out in the inner product of $\ln\bar{\mathbf{B}}_e$ with $\overline{\ln\bar{\mathbf{B}}_e}^{\,\cdot}$.

By substituting Eq. (6) into Eq. (31), one obtains

$$\dot{\gamma}_1 = 2\mathbf{E}'_e \cdot (\mathbf{D}' - \mathbf{D}_p)\,,$$

such that Eq. (26) implies

$$\mathbf{T}' = \mathbf{M} = \frac{2\mu}{J}\mathbf{E}'_e\,. \tag{32}$$

2.4. Particularization to conventional finite-deformation elastoplasticity

In general, the particularization to size-independent finite-deformation elastoplasticity is obtained by setting $\ell = 0$, thus imposing that the defect stress vanishes (see, e.g., Eq. (21)). Within the present DGP theory, the skew-symmetric part of the higher-order balance law (14) then yields $\mathbf{S}_{\rm W} = \mathbf{0}$, thus implying $\mathbf{W}_p = \mathbf{0}$ through Eq. (23), and the symmetric part of the higher-order balance law (14) specializes to

$$\mathbf{S}_{\rm D} \equiv \sqrt{\frac{2}{3}}SV(d_p)\frac{\mathbf{D}_p}{|\mathbf{D}_p|} = \mathbf{M}\,,$$

where use has been made of the constitutive Eq. (23). This relation gives $\mathbf{D}_p$ as a function of $\bar{\mathbf{B}}_e$ which is dependent on the form of $\mathbf{M}$. In turn, this expression for $\mathbf{D}_p$, along with $\mathbf{W}_p = \mathbf{0}$, has then to be substituted into the equation for $\mathbf{A}$ (see, e.g., Eq. (5)) in order to obtain the evolution equation for $\bar{\mathbf{B}}_e$ for size-independent elastoplasticity.

2.5. Higher-order equations governing plane-strain boundary value problems

This work discusses the results of the proposed theory by focusing on plane-strain boundary value problems, thus allowing a much less demanding FE implementation, provided in next Section 3, than that required for general three-dimensional problems. In the kinematic approach followed here, the key issue is the capability to correctly satisfy the minimum continuity requirements of $\mathbf{L}_p$, consistently with the structure of the higher-order boundary conditions (15). This issue is addressed by the use of $H(\mathrm{curl})$ FEs.

By referring to a fixed rectangular Cartesian reference system (x_1, x_2, x_3) for the current configuration, with out-of-plane axis $x_3 \equiv X_3$ (i.e. constant out-of-plane normal), the matrix form of $\mathrm{curl}\,\mathbf{L}_p$ reads

$$[\mathrm{curl}\,\mathbf{L}_p] = \begin{bmatrix} 0 & 0 & L_{p12,1} - L_{p11,2} \\ 0 & 0 & L_{p22,1} - L_{p21,2} \\ L_{p33,2} & -L_{p33,1} & 0 \end{bmatrix}, \tag{33}$$

which has to satisfy the condition $\mathrm{tr}(\mathbf{L}_p) = 0$.

The microhard boundary conditions (15) are conveniently specified in terms of the in-plane vectors

$$\mathbf{L}_{p1}^T = [L_{p11}\;\; L_{p12}]\,, \quad \mathbf{L}_{p2}^T = [L_{p21}\;\; L_{p22}] \tag{34}$$

as Panteghini and Bardella (2018)

$$\mathbf{L}_{p1} \cdot \mathbf{t} = 0\,, \quad \mathbf{L}_{p2} \cdot \mathbf{t} = 0\,, \quad L_{p33} = 0\,, \tag{35}$$

where $\mathbf{t}$ is the 2D unit vector tangential to the boundary.

From inspection of Eqs. (2) and (33), it is deduced that the sole non-vanishing components of $\boldsymbol{\alpha}$ are α_{13}, α_{23}, α_{31}, and α_{32}, as

$$[\dot{\boldsymbol{\alpha}}] = \begin{bmatrix} 0 & 0 & \Omega_{12}\alpha_{23} \\ 0 & 0 & -\Omega_{12}\alpha_{13} \\ \Omega_{12}\alpha_{32} & -\Omega_{12}\alpha_{31} & 0 \end{bmatrix} + \begin{bmatrix} 0 & 0 & L_{p12},_1 - L_{p11},_2 \\ 0 & 0 & L_{p22},_1 - L_{p21},_2 \\ L_{p33},_2 & -L_{p33},_1 & 0 \end{bmatrix}. \tag{36}$$

On the basis of Eq. (36), the sole non-vanishing components of the curl of the defect stress are

$$[\mathrm{curl}\,\boldsymbol{\zeta}] = \mu\ell^2 \begin{bmatrix} (\frac{\alpha_{13}}{J}),_2 & -(\frac{\alpha_{13}}{J}),_1 & 0 \\ (\frac{\alpha_{23}}{J}),_2 & -(\frac{\alpha_{23}}{J}),_1 & 0 \\ 0 & 0 & (\frac{\alpha_{32}}{J}),_1 - (\frac{\alpha_{31}}{J}),_2 \end{bmatrix}. \tag{37}$$

Therefore, by using the constitutive Eqs. (21) and (23), the sole non-vanishing PDE of the skew-symmetric part of the higher-order balance law (14) is

$$\chi S V(d_p) \frac{W_{p12}}{d_p} = \frac{\mu\ell^2}{2} \left[(\frac{\alpha_{13}}{J}),_1 + (\frac{\alpha_{23}}{J}),_2 \right], \tag{38}$$

while the non-vanishing PDEs of the symmetric part of the higher-order balance law (14) are

$$\begin{aligned} M_{11} &= \frac{2}{3} S V(d_p) \frac{D_{p11}}{d_p} + \frac{\mu\ell^2}{3} \left[2(\frac{\alpha_{13}}{J}),_2 + (\frac{\alpha_{23}}{J}),_1 - (\frac{\alpha_{32}}{J}),_1 + (\frac{\alpha_{31}}{J}),_2 \right], \\ M_{22} &= \frac{2}{3} S V(d_p) \frac{D_{p22}}{d_p} + \frac{\mu\ell^2}{3} \left[-2(\frac{\alpha_{23}}{J}),_1 - (\frac{\alpha_{13}}{J}),_2 - (\frac{\alpha_{32}}{J}),_1 + (\frac{\alpha_{31}}{J}),_2 \right], \\ M_{33} &= \frac{2}{3} S V(d_p) \frac{D_{p33}}{d_p} + \frac{\mu\ell^2}{3} \left[2(\frac{\alpha_{32}}{J}),_1 - 2(\frac{\alpha_{31}}{J}),_2 - (\frac{\alpha_{13}}{J}),_2 + (\frac{\alpha_{23}}{J}),_1 \right], \\ M_{12} &= \frac{2}{3} S V(d_p) \frac{D_{p12}}{d_p} + \frac{\mu\ell^2}{2} \left[(\frac{\alpha_{23}}{J}),_2 - (\frac{\alpha_{13}}{J}),_1 \right]. \end{aligned} \tag{39}$$

The foregoing equations will be useful to discuss the numerical results presented in Section 4.

3. The $H(\mathrm{curl})$ finite element formulation for plane-strain boundary value problems

The FE implementation of higher-order DGP relying on the Nye-Kröner tensor requires the use of $H(\mathrm{curl})$ FEs, whose development started with the need to solve the Maxwell equations governing boundary value problems in electromagnetism (Nédélec, 1980; Jin, 2014).

The technique adopted to formulate an $H(\mathrm{curl})$ field (Rognes et al., 2010; Wieners and Wohlmuth, 2011) for the plastic distortion rate $\mathbf{L}_p$ does not ensure that the resulting discretized field $\mathbf{L}_p$ is isochoric. This issue is addressed by enforcing the condition $\mathrm{tr}(\mathbf{L}_p) = 0$ in a weak form, through the Lagrange multiplier λ, such that the internal virtual power, for general three-dimensional stress and strain fields, assumes the form

$$\delta W_i = \int_P \left[\mathbf{T} \cdot \delta\mathbf{D} + \mathbf{S} \cdot \delta\mathbf{L}_p - \mathbf{M} \cdot \delta\mathbf{D}_p + \lambda\, \mathrm{tr}(\delta\mathbf{L}_p) + \boldsymbol{\zeta} \cdot \delta\big(\mathrm{curl}\,\mathbf{L}_p\big) + \mathrm{tr}(\mathbf{L}_p)\, \delta\lambda \right] \mathrm{d}V\,,$$

where P is an arbitrary subregion of the body in the current configuration.

With this approach, $\delta\mathbf{L}_p$ does not need to be traceless anymore and, importantly, $\mathbf{S}$ is computed by substituting in the constitutive Eqs. (23) the deviatoric part of the current $\mathbf{L}_p$, i.e. $\mathbf{L}'_p$, so that $\mathrm{tr}(\mathbf{S}) = 0$ always in the following. The constraint equation associated with λ enforces $\mathrm{tr}(\mathbf{L}_p) = 0$ at convergence, thereby ensuring an isochoric plastic distortion rate.

The proposed 2D quadrilateral FE for plane deformations has 4 nodes, linear shape functions, and twenty-four DOFs overall. Each node has four DOFs, consisting of the two displacement components u_1 and u_2, the out-of-plane plastic rate L_{p33}, and the Lagrange multiplier λ, whereas each edge has two DOFs, consisting of the edge-averaged values of the tangential components of the vectors $\mathbf{L}_{p1}$ and $\mathbf{L}_{p2}$ in Eq. (34) (Panteghini and Bardella, 2018). [2] Full integration, corresponding to a 2×2 Gauss quadrature rule, is always adopted.

[2] A fully three-dimensional hexahedral counterpart of the present FE would have 68 DOFs overall: four nodal DOFs at each of the eight nodes, namely u_1, u_2, u_3, and λ, plus three $H(\mathrm{curl})$ edge DOFs on each of the twelve edges, corresponding to the edge-averaged tangential components of the three vectors $\mathbf{L}^T_{p1} = [L_{p11}\ L_{p12}\ L_{p13}]$, $\mathbf{L}^T_{p2} = [L_{p21}\ L_{p22}\ L_{p23}]$, and $\mathbf{L}^T_{p3} = [L_{p31}\ L_{p32}\ L_{p33}]$. For a plane-strain restriction with out-of-plane edges aligned with the x_3 direction, the in-plane edge DOFs are retained for $\mathbf{L}_{p1}$ and $\mathbf{L}_{p2}$ (see Eqs. (34) and (35)), whereas the edge DOFs associated with the out-of-plane edges of $\mathbf{L}_{p3}$ are represented in the reduced two-dimensional setting by the nodal values of L_{p33}. For each vector of $\mathbf{L}_p$, the $H(\mathrm{curl})$ discretization provides a well-defined tangential trace on element faces and enforces the continuity of this tangential trace across interelement faces (Jin, 2014). The normal component, instead, is not required to be continuous.

Isoparametric FEs are employed, so that the shape functions also linearly interpolate the *reference* geometry and are specified by

$$\mathbf{x}_R = \mathbf{N}_R(r,s)\,\hat{\mathbf{x}}_R\,,$$

where

$$\mathbf{N}_R(r,s) = \begin{bmatrix} N_R^{(1)}(r,s) & 0 & N_R^{(2)}(r,s) & 0 & N_R^{(3)}(r,s) & 0 & N_R^{(4)}(r,s) & 0 \\ 0 & N_R^{(1)}(r,s) & 0 & N_R^{(2)}(r,s) & 0 & N_R^{(3)}(r,s) & 0 & N_R^{(4)}(r,s) \end{bmatrix},$$

$$N_R^{(1)}(r,s) = \frac{1}{4}(1-r)(1-s)\,, \qquad N_R^{(2)}(r,s) = \frac{1}{4}(1+r)(1-s)\,,$$

$$N_R^{(3)}(r,s) = \frac{1}{4}(1+r)(1+s)\,, \qquad N_R^{(4)}(r,s) = \frac{1}{4}(1-r)(1+s)\,,$$

$$\hat{\mathbf{x}}_R = \begin{bmatrix} \hat{x}_{R,1}^{(1)} & \hat{x}_{R,2}^{(1)} & \hat{x}_{R,1}^{(2)} & \hat{x}_{R,2}^{(2)} & \hat{x}_{R,1}^{(3)} & \hat{x}_{R,2}^{(3)} & \hat{x}_{R,1}^{(4)} & \hat{x}_{R,2}^{(4)} \end{bmatrix}^T,$$

$(\hat{x}_{R,1}^{(k)}, \hat{x}_{R,2}^{(k)})$ are the *reference* (initial) coordinates of the node k, $r \in [-1,1]$ and $s \in [-1,1]$ are the intrinsic coordinates, and $\mathbf{x}_R = \begin{bmatrix} x_{R,1} & x_{R,2} \end{bmatrix}^T$.

The derivatives of the shape functions with respect to the reference coordinate system are computed as

$$\mathbf{H}_R = \begin{bmatrix} \frac{\partial N^{(1)}}{\partial x_{R,1}} & \frac{\partial N^{(2)}}{\partial x_{R,1}} & \frac{\partial N^{(3)}}{\partial x_{R,1}} & \frac{\partial N^{(4)}}{\partial x_{R,1}} \\ \frac{\partial N^{(1)}}{\partial x_{R,2}} & \frac{\partial N^{(2)}}{\partial x_{R,2}} & \frac{\partial N^{(3)}}{\partial x_{R,2}} & \frac{\partial N^{(4)}}{\partial x_{R,2}} \end{bmatrix} = \mathbf{J}_R^{-1}\mathbf{H}_p\,,$$

where $\mathbf{H}_p$ is the matrix that contains the derivatives of the shape functions with respect to r and s, i.e.

$$\mathbf{H}_p = \begin{bmatrix} \frac{\partial N^{(1)}}{\partial r} & \frac{\partial N^{(2)}}{\partial r} & \frac{\partial N^{(3)}}{\partial r} & \frac{\partial N^{(4)}}{\partial r} \\ \frac{\partial N^{(1)}}{\partial s} & \frac{\partial N^{(2)}}{\partial s} & \frac{\partial N^{(3)}}{\partial s} & \frac{\partial N^{(4)}}{\partial s} \end{bmatrix} = \frac{1}{4}\begin{bmatrix} s-1 & 1-s & 1+s & -1-s \\ r-1 & -1-r & 1+r & 1-r \end{bmatrix},$$

and

$$\mathbf{J}_R = \mathbf{H}_p\hat{\mathbf{X}}_R\,,$$

with

$$\hat{\mathbf{X}}_R = \begin{bmatrix} \hat{x}_{R,1}^{(1)} & \hat{x}_{R,2}^{(1)} \\ \hat{x}_{R,1}^{(2)} & \hat{x}_{R,2}^{(2)} \\ \hat{x}_{R,1}^{(3)} & \hat{x}_{R,2}^{(3)} \\ \hat{x}_{R,1}^{(4)} & \hat{x}_{R,2}^{(4)} \end{bmatrix}.$$

Then, the displacement field $\mathbf{u}$, the out-of-plane plastic rate L_{p33}, and the Lagrange multiplier λ are discretized with respect to the reference configuration as

$$\mathbf{u}(r,s) = \mathbf{N}_R(r,s)\,\hat{\mathbf{u}}\,, \quad L_{p33}(r,s) = \mathbf{N}_{Rs}^T(r,s)\,\hat{\mathbf{L}}_{p33}\,, \quad \lambda(r,s) = \mathbf{N}_{Rs}^T(r,s)\,\hat{\lambda}\,,$$

where

$$\hat{\mathbf{u}} = \begin{bmatrix} \hat{u}_1^{(1)} & \hat{u}_2^{(1)} & \hat{u}_1^{(2)} & \hat{u}_2^{(2)} & \hat{u}_1^{(3)} & \hat{u}_2^{(3)} & \hat{u}_1^{(4)} & \hat{u}_2^{(4)} \end{bmatrix}^T,$$

$$\mathbf{N}_{Rs}(r,s) = \begin{bmatrix} N_R^{(1)}(r,s) & N_R^{(2)}(r,s) & N_R^{(3)}(r,s) & N_R^{(4)}(r,s), \end{bmatrix}^T,$$

$$\hat{\mathbf{L}}_{p33} = \begin{bmatrix} \hat{L}_{p33}^{(1)} & \hat{L}_{p33}^{(2)} & \hat{L}_{p33}^{(3)} & \hat{L}_{p33}^{(4)} \end{bmatrix}^T,$$

$$\hat{\lambda} = \begin{bmatrix} \hat{\lambda}^{(1)} & \hat{\lambda}^{(2)} & \hat{\lambda}^{(3)} & \hat{\lambda}^{(4)} \end{bmatrix}^T,$$

with $\hat{\mathbf{u}}$, $\hat{\mathbf{L}}_{p33}$, and $\hat{\lambda}$ denoting the vectors containing the FE DOFs.

Under these assumptions, the deformation gradient $\mathbf{F}(t_{n+1}) = \mathbf{F}_{n+1} = \mathbf{F}$ at the end of a generic step at the time t_{n+1}, stored in array notation,[3] is computed in terms of the nodal displacement components as

$$\mathbf{F} = \mathbf{I} + \mathrm{Grad}\,\mathbf{u} = \mathbf{I} + \mathcal{A}(\mathbf{H}_R)\,\hat{\mathbf{u}}\,,$$

[3] At the implementation level, the components of each second-order 2D tensor (symmetric or non-symmetric) are stored in a 5-component vector. For instance,

$$[\mathbf{F}] = \begin{bmatrix} F_{11} & F_{12} & 0 \\ F_{21} & F_{22} & 0 \\ 0 & 0 & F_{33} \end{bmatrix} \rightarrow \mathbf{F} = \begin{bmatrix} F_{11} \\ F_{22} \\ F_{33} \\ F_{12} \\ F_{21} \end{bmatrix}, \qquad \mathbf{I} = \begin{bmatrix} 1 \\ 1 \\ 1 \\ 0 \\ 0 \end{bmatrix}.$$

where $\mathbf{I}$ is the second-order identity tensor and $\mathcal{A}(\mathbf{H}_R)$ is a linear function that maps the components of $\mathbf{H}_R$ into the 5x8 matrix

$$\mathcal{A}(\mathbf{H}_R) = \begin{bmatrix} (\mathbf{H}_R)_{11} & 0 & (\mathbf{H}_R)_{12} & 0 & (\mathbf{H}_R)_{13} & 0 & (\mathbf{H}_R)_{14} & 0 \\ 0 & (\mathbf{H}_R)_{21} & 0 & (\mathbf{H}_R)_{22} & 0 & (\mathbf{H}_R)_{23} & 0 & (\mathbf{H}_R)_{24} \\ 0 & 0 & 0 & 0 & 0 & 0 & 0 & 0 \\ (\mathbf{H}_R)_{21} & 0 & (\mathbf{H}_R)_{22} & 0 & (\mathbf{H}_R)_{23} & 0 & (\mathbf{H}_R)_{24} & 0 \\ 0 & (\mathbf{H}_R)_{11} & 0 & (\mathbf{H}_R)_{12} & 0 & (\mathbf{H}_R)_{13} & 0 & (\mathbf{H}_R)_{14} \end{bmatrix}.$$

The derivatives of the shape functions with respect to the *current* coordinates can now be computed as

$$\mathbf{H} = \begin{bmatrix} \frac{\partial N^{(1)}}{\partial x_1} & \frac{\partial N^{(2)}}{\partial x_1} & \frac{\partial N^{(3)}}{\partial x_1} & \frac{\partial N^{(4)}}{\partial x_1} \\ \frac{\partial N^{(1)}}{\partial x_2} & \frac{\partial N^{(2)}}{\partial x_2} & \frac{\partial N^{(3)}}{\partial x_2} & \frac{\partial N^{(4)}}{\partial x_2} \end{bmatrix} = \mathbf{J}^{-1}\mathbf{H}_p \,,$$

where

$$\mathbf{J} = \mathbf{J}_R \mathbf{F}^T \,, \quad \mathbf{J}^{-1} = \mathbf{F}^{-T}\mathbf{J}_R^{-1} \,.$$

The total deformation rate $\mathbf{D}$ is computed in terms of the rates of the nodal displacement components as

$$\mathbf{D} = \mathcal{B}(\mathbf{H})\,\dot{\hat{\mathbf{u}}} \,,$$

where $\mathcal{B}(\mathbf{H})$ is a linear function that maps the components of the matrix $\mathbf{H}$ into the 5x8 matrix

$$\mathcal{B}(\mathbf{H}) = \begin{bmatrix} H_{11} & 0 & H_{12} & 0 & H_{13} & 0 & H_{14} & 0 \\ 0 & H_{21} & 0 & H_{22} & 0 & H_{23} & 0 & H_{24} \\ 0 & 0 & 0 & 0 & 0 & 0 & 0 & 0 \\ \frac{1}{2}H_{21} & \frac{1}{2}H_{11} & \frac{1}{2}H_{22} & \frac{1}{2}H_{12} & \frac{1}{2}H_{23} & \frac{1}{2}H_{13} & \frac{1}{2}H_{24} & \frac{1}{2}H_{14} \\ \frac{1}{2}H_{21} & \frac{1}{2}H_{11} & \frac{1}{2}H_{22} & \frac{1}{2}H_{12} & \frac{1}{2}H_{23} & \frac{1}{2}H_{13} & \frac{1}{2}H_{24} & \frac{1}{2}H_{14} \end{bmatrix}.$$

By following Panteghini and Bardella (2018), the plastic distortion rate $\mathbf{L}_p$ is discretized by defining a vector basis $\mathbf{V}^{(i)}$, $i = 1, 2, 3, 4$, that ensures curl conformity. Hence, this vector basis is constructed so that the edge degrees of freedom represent the tangential components of $\mathbf{L}_p$ along the FE edges in *current* configuration are constrained to be continuous, thereby enforcing the continuity of the tangential trace across interelement boundaries. To this purpose, the required DOFs are related to the in-plane vectors defined in Eq. (34), whose discretization is proposed in the form

$$\mathbf{L}_{p1} = \sum_{i=1}^{4} \mathbf{V}^{(i)} \hat{L}_{p1t}^{(i)} \,, \quad \mathbf{L}_{p2} = \sum_{i=1}^{4} \mathbf{V}^{(i)} \hat{L}_{p2t}^{(i)} \,,$$

where, for a given i, $\mathbf{V}^{(i)}$ has vanishing tangential component along all the FE edges except for the i−th edge and the scalars DOFs $\hat{L}_{p1t}^{(i)}$ and $\hat{L}_{p2t}^{(i)}$ are the *average* value of the tangential components of $\mathbf{L}_{p1}$ and $\mathbf{L}_{p2}$, respectively, along the i−th FE edge. Each vector basis $\mathbf{V}^{(i)}$, $i = 1, 2, 3, 4$, is a function of the current FE edges' lengths, denoted as $h_e^{(i)}$, and of the deformation gradient $\mathbf{F}$ through the jacobian in current configuration $\mathbf{J}$. The i-th vector of the basis can be expressed as

$$\mathbf{V}^{(i)}(\mathbf{J}, h_e^{(i)}) = h_e^{(i)} \mathbf{v}^{(i)}(\mathbf{J}) \,,$$

where

$$\mathbf{J}^{-1} \equiv \begin{bmatrix} \operatorname{grad} r & \operatorname{grad} s \end{bmatrix} \,,$$

with grad denoting the *in-plane* gradient operator with respect to the current configuration.

By following Panteghini and Bardella (2018), the vector basis is rewritten as

$$\begin{aligned} \left[\mathbf{v}^{(1)}(\mathbf{J})\right]_i &= \frac{1}{4}(1-s)(\operatorname{grad} r)_i = \frac{1}{4}(1-s)\left(\mathbf{J}^{-1}\right)_{i1} \,, \\ \left[\mathbf{v}^{(2)}(\mathbf{J})\right]_i &= \frac{1}{4}(1+r)(\operatorname{grad} s)_i = \frac{1}{4}(1+r)\left(\mathbf{J}^{-1}\right)_{i2} \,, \\ \left[\mathbf{v}^{(3)}(\mathbf{J})\right]_i &= \frac{1}{4}(1+s)(\operatorname{grad} r)_i = \frac{1}{4}(1+s)\left(\mathbf{J}^{-1}\right)_{i1} \,, \\ \left[\mathbf{v}^{(4)}(\mathbf{J})\right]_i &= \frac{1}{4}(1-r)(\operatorname{grad} s)_i = \frac{1}{4}(1-r)\left(\mathbf{J}^{-1}\right)_{i2} \,, \end{aligned} \tag{40}$$

where $(\mathbf{J}^{-1})_{ij}$ denotes i, j component of the 2×2 matrix $\mathbf{J}^{-1}$.

Hence, the plastic deformation rate is computed as

$$\mathbf{D}_p = \begin{bmatrix} L_{p11} \\ L_{p22} \\ L_{p33} \\ \frac{1}{2}\left(L_{p12} + L_{p21}\right) \\ \frac{1}{2}\left(L_{p12} + L_{p21}\right) \end{bmatrix} = \mathcal{E}_t(h_e^{(i)}, \mathbf{v}^{(i)})\,\hat{\mathbf{L}}_{p_t} + \boldsymbol{E}_z \hat{\mathbf{L}}_{p33} \,,$$

where

$$\hat{\mathbf{L}}_{pt} = \begin{bmatrix} \hat{L}^{(1)}_{p1t} & \hat{L}^{(1)}_{p2t} & \hat{L}^{(2)}_{p1t} & \hat{L}^{(2)}_{p2t} & \hat{L}^{(3)}_{p1t} & \hat{L}^{(3)}_{p2t} & \hat{L}^{(4)}_{p1t} & \hat{L}^{(4)}_{p2t} \end{bmatrix}^T ,$$

$$\boldsymbol{E}_z = \begin{bmatrix} 0 & 0 & 0 & 0 \\ 0 & 0 & 0 & 0 \\ N^{(1)}_R & N^{(2)}_R & N^{(3)}_R & N^{(4)}_R \\ 0 & 0 & 0 & 0 \\ 0 & 0 & 0 & 0 \end{bmatrix},$$

and $\mathcal{E}_t(h^{(i)}_e, \mathbf{v}^{(i)})$ is a linear function that maps the current edge length $h^{(i)}_e$ and the vector basis $\mathbf{v}^{(i)}$ into the 5x8 matrix

$$\mathcal{E}_t(h^{(i)}_e, \mathbf{v}^{(i)}) = \begin{bmatrix} h^{(1)}_e v^{(1)}_1 & 0 & h^{(2)}_e v^{(2)}_1 & 0 & h^{(3)}_e v^{(3)}_1 & 0 & h^{(4)}_e v^{(4)}_1 & 0 \\ 0 & h^{(1)}_e v^{(1)}_2 & 0 & h^{(2)}_e v^{(2)}_2 & 0 & h^{(3)}_e v^{(3)}_2 & 0 & h^{(4)}_e v^{(4)}_2 \\ 0 & 0 & 0 & 0 & 0 & 0 & 0 & 0 \\ \frac{1}{2} h^{(1)}_e v^{(1)}_2 & \frac{1}{2} h^{(1)}_e v^{(1)}_1 & \frac{1}{2} h^{(2)}_e v^{(2)}_2 & \frac{1}{2} h^{(2)}_e v^{(2)}_1 & \frac{1}{2} h^{(3)}_e v^{(3)}_2 & \frac{1}{2} h^{(3)}_e v^{(3)}_1 & \frac{1}{2} h^{(4)}_e v^{(4)}_2 & \frac{1}{2} h^{(4)}_e v^{(4)}_1 \\ \frac{1}{2} h^{(1)}_e v^{(1)}_2 & \frac{1}{2} h^{(1)}_e v^{(1)}_1 & \frac{1}{2} h^{(2)}_e v^{(2)}_2 & \frac{1}{2} h^{(2)}_e v^{(2)}_1 & \frac{1}{2} h^{(3)}_e v^{(3)}_2 & \frac{1}{2} h^{(3)}_e v^{(3)}_1 & \frac{1}{2} h^{(4)}_e v^{(4)}_2 & \frac{1}{2} h^{(4)}_e v^{(4)}_1 \end{bmatrix}.$$

The computation of the dissipative stresses requires also the plastic spin rate W_{p12}, which is obtained as

$$W_{p12} = \mathcal{E}_{\mathcal{SK}}(h^{(i)}_e, \mathbf{v}^{(i)})^T \hat{\mathbf{L}}_{pt} ,$$

where $\mathcal{E}_{\mathcal{SK}}(h^{(i)}_e, \mathbf{v}^{(i)})$ is a linear function that maps the current edge length $h^{(i)}_e$ and the vector basis $\mathbf{v}^{(i)}$ into the 8-component vector

$$\mathcal{E}_{\mathcal{SK}}(h^{(i)}_e, \mathbf{v}^{(i)}) = \frac{1}{2} \begin{bmatrix} h^{(1)}_e v^{(1)}_2 & -h^{(1)}_e v^{(1)}_1 & h^{(2)}_e v^{(2)}_2 & -h^{(2)}_e v^{(2)}_1 & h^{(3)}_e v^{(3)}_2 & -h^{(3)}_e v^{(3)}_1 & h^{(4)}_e v^{(4)}_2 & -h^{(4)}_e v^{(4)}_1 \end{bmatrix}^T .$$

To compute the HO recoverable term of the internal power, it is convenient to define the following array form of $\mathrm{curl}\,\mathbf{L}_p$ in Eq. (33)

$$[\mathrm{curl}\,\mathbf{L}_p] = \begin{bmatrix} 0 & 0 & (\mathrm{curl}\,\mathbf{L}_p)_{13} \\ 0 & 0 & (\mathrm{curl}\,\mathbf{L}_p)_{23} \\ (\mathrm{curl}\,\mathbf{L}_p)_{31} & (\mathrm{curl}\,\mathbf{L}_p)_{32} & 0 \end{bmatrix} \to \mathrm{curl}\,\mathbf{L}_p = \begin{bmatrix} (\mathrm{curl}\,\mathbf{L}_p)_{13} \\ (\mathrm{curl}\,\mathbf{L}_p)_{23} \\ (\mathrm{curl}\,\mathbf{L}_p)_{31} \\ (\mathrm{curl}\,\mathbf{L}_p)_{32} \end{bmatrix} = \begin{bmatrix} (\mathrm{curl}\,\mathbf{L}_{p1})^T \mathbf{e}_3 \\ (\mathrm{curl}\,\mathbf{L}_{p2})^T \mathbf{e}_3 \\ \partial L_{p33}/\partial x_2 \\ -\partial L_{p33}/\partial x_1 \end{bmatrix}, \tag{41}$$

where $\mathbf{e}_3$ denotes the unit vector along the out-of-plane direction and taking the curl of the 2-component vectors $\mathbf{L}_{p1}$ and $\mathbf{L}_{p2}$ requires knowledge that their out-of-plane derivative and their out-of-plane component are zero.

Although the curl operator is defined in terms of the spatial derivatives reported in Eq. (33), in the present $H(\mathrm{curl})$ discretization the first two components of the array in Eq. (41) are not computed by differentiating a standard nodal interpolation of the components of $\mathbf{L}_p$. Instead, following Panteghini and Bardella (2018), the vector fields $\mathbf{L}_{p1}$ and $\mathbf{L}_{p2}$ are interpolated directly by means of edge-based $H(\mathrm{curl})$ basis functions, so that their discrete curls are obtained as

$$\mathrm{curl}\,\mathbf{L}_{p1} = \sum_{i=1}^{4} \hat{L}^{(i)}_{p1t} \left(\mathrm{curl}\,\mathbf{V}^{(i)}\right) = \sum_{i=1}^{4} h^{(i)}_e \hat{L}^{(i)}_{p1t} \left(\mathrm{curl}\,\mathbf{v}^{(i)}\right) ,$$

$$\mathrm{curl}\,\mathbf{L}_{p2} = \sum_{i=1}^{4} \hat{L}^{(i)}_{p2t} \left(\mathrm{curl}\,\mathbf{V}^{(i)}\right) = \sum_{i=1}^{4} h^{(i)}_e \hat{L}^{(i)}_{p2t} \left(\mathrm{curl}\,\mathbf{v}^{(i)}\right) .$$

By using Eq. (40) and the properties of the curl and grad operators, it can be shown that

$$\mathrm{curl}\,\mathbf{v}^{(1)} = \mathrm{curl}\,\mathbf{v}^{(2)} = \frac{1}{4} (\mathrm{grad}\, r) \times (\mathrm{grad}\, s) = \frac{1}{4(\det \mathbf{J})} \mathbf{e}_3 , \tag{42}$$

$$\mathrm{curl}\,\mathbf{v}^{(3)} = \mathrm{curl}\,\mathbf{v}^{(4)} = \frac{1}{4} (\mathrm{grad}\, s) \times (\mathrm{grad}\, r) = -\frac{1}{4(\det \mathbf{J})} \mathbf{e}_3 . \tag{43}$$

Hence, by using Eqs. (42) and (43), Eq. (41) can be discretized as

$$\mathrm{curl}\,\mathbf{L}_p = \mathcal{C}_t(h^{(i)}_e, J) \hat{\mathbf{L}}_{pt} + \mathcal{C}_z(\mathbf{H}) \hat{\mathbf{L}}_{p33} , \tag{44}$$

where $\mathcal{C}_t(h^{(i)}_e, J)$ is a linear function that maps $J = \det \mathbf{F}$ and $h^{(i)}_e$ into the 4x8 matrix

$$\mathcal{C}_t(h^{(i)}_e, J) = \frac{1}{4J \det \mathbf{J}_R} \begin{bmatrix} h^{(1)}_e & 0 & h^{(2)}_e & 0 & -h^{(3)}_e & 0 & -h^{(4)}_e & 0 \\ 0 & h^{(1)}_e & 0 & h^{(2)}_e & 0 & -h^{(3)}_e & 0 & -h^{(4)}_e \\ 0 & 0 & 0 & 0 & 0 & 0 & 0 & 0 \\ 0 & 0 & 0 & 0 & 0 & 0 & 0 & 0 \end{bmatrix}$$

and $\mathcal{C}_z(\mathbf{H})$ is a linear function that maps the derivatives of the shape function with respect to the current coordinate system into the 4x4 matrix

$$\mathcal{C}_z(\mathbf{H}) = \begin{bmatrix} 0 & 0 & 0 & 0 \\ 0 & 0 & 0 & 0 \\ H_{21} & H_{22} & H_{23} & H_{24} \\ -H_{11} & -H_{12} & -H_{13} & -H_{14} \end{bmatrix}.$$

The following operators are used to discretize the internal virtual power, in the reference configuration, as

$$\delta W_i = \int_{P_0} \delta\hat{\mathbf{u}}^T \left(\mathcal{B}(\mathbf{H})^T \mathbf{T}\right) J \,\mathrm{d}V + \int_{P_0} \delta\hat{\mathbf{L}}_{pt}^T \left[\mathcal{E}_t(h_e^{(i)}, \mathbf{v}^{(i)})^T \left(\mathbf{S}_\mathrm{D} - \mathbf{M} + \lambda\mathbf{I}\right) + 2\,\mathcal{E}_{S\mathcal{K}}(h_e^{(i)}, \mathbf{v}^{(i)})\, S_{\mathrm{W}\,12} + \mathcal{C}_t(h_e^{(i)}, J)^T \zeta\right] J \,\mathrm{d}V$$
$$+ \int_{P_0} \delta\hat{\mathbf{L}}_{p33}^T \left[\boldsymbol{E}_z^T \left(\mathbf{S}_\mathrm{D} - \mathbf{M} + \lambda\mathbf{I}\right) + \mathcal{C}_z(\mathbf{H})^T \zeta\right] J \,\mathrm{d}V + \int_{P_0} \delta\hat{\lambda}^T \mathbf{N}_{Rs} \mathrm{tr}(\mathbf{L}_p) J \,\mathrm{d}V \,. \tag{45}$$

Differentiation of Eq. (45) with respect to the variation of the DOFs $\delta\hat{\mathbf{u}}$, $\delta\hat{\mathbf{L}}_{pt}$, $\delta\hat{\mathbf{L}}_{p33}$, and $\delta\hat{\lambda}$ gives the internal generalized forces associated with the element DOFs, employed to check if equilibrium in achieved in the current step increment. They result

$$\mathbf{F}_u^{int} = \int_{P_0} \left(\mathcal{B}(\mathbf{H})^T \mathbf{T}\right) J \,\mathrm{d}V \,,$$
$$\mathbf{F}_{Lpt}^{int} = \int_{P_0} \left[\mathcal{E}_t(h_e^{(i)}, \mathbf{v}^{(i)})^T \left(\mathbf{S}_\mathrm{D} - \mathbf{M} + \lambda\mathbf{I}\right) + 2\,\mathcal{E}_{S\mathcal{K}}(h_e^{(i)}, \mathbf{v}^{(i)})\, S_{\mathrm{W}\,12} + \mathcal{C}_t(h_e^{(i)}, J)^T \zeta\right] J \,\mathrm{d}V \,,$$
$$\mathbf{F}_{Lp33}^{int} = \int_{P_0} \left[\boldsymbol{E}_z^T \left(\mathbf{S}_\mathrm{D} - \mathbf{M} + \lambda\mathbf{I}\right) + \mathcal{C}_z(\mathbf{H})^T \zeta\right] J \,\mathrm{d}V \,,$$
$$\mathbf{F}_\lambda^{int} = \int_{P_0} \mathbf{N}_{Rs} \mathrm{tr}(\mathbf{L}_p) J \,\mathrm{d}V \,.$$

3.1. Time-integration of the elastic left Cauchy-Green tensor

The deformation gradient $\mathbf{F} = \mathbf{F}_{n+1}$ at the end of a generic step at the time t_{n+1} is written in terms of the deformation gradient $\mathbf{F}_n$ at the time t_n and of the relative deformation gradient $\mathbf{F}_\Delta$ (Simo, 1992) as

$$\mathbf{F} = \mathbf{F}_\Delta \mathbf{F}_n \,,$$

so that

$$\mathbf{F}_\Delta = \mathbf{F}\,\mathbf{F}_n^{-1} \,.$$

Given that the volumetric response is purely elastic (see Eq. (11)), one has

$$J_e = J = J_\Delta J_n$$

where $J_\Delta = \det \mathbf{F}_\Delta$ and J_n is the total dilatation at the time t_n.

Since $\dot{\mathbf{F}} = \mathbf{L}\,\mathbf{F}$, the relative deformation gradient satisfies the evolution equation

$$\dot{\mathbf{F}}_\Delta = \dot{\mathbf{F}}\,\mathbf{F}_n^{-1} = \mathbf{L}\,\mathbf{F}\,\mathbf{F}_n^{-1} = \mathbf{L}\,\mathbf{F}_\Delta \,, \quad \mathbf{F}_\Delta(t_n) = \mathbf{I} \,.$$

The unimodular (distortional) part of $\mathbf{F}_\Delta$ is computed as

$$\bar{\mathbf{F}}_\Delta = (J_\Delta)^{-1/3} \mathbf{F}_\Delta \,, \qquad \det \bar{\mathbf{F}}_\Delta = 1 \,.$$

In general, the deviatoric part of the velocity gradient $\mathbf{L}' = \mathbf{L}'(t)$ varies within the time increment. It is assumed that $\mathbf{L}'(t)$ can be approximated by the constant step-average $\tilde{\mathbf{L}}'$, so that the evolution Eq. (46) is written as

$$\dot{\bar{\mathbf{F}}}_\Delta = \tilde{\mathbf{L}}'\,\bar{\mathbf{F}}_\Delta \,, \qquad \bar{\mathbf{F}}_\Delta(t_n) = \mathbf{I} \,. \tag{46}$$

The exact solution of Eq. (46) is

$$\bar{\mathbf{F}}_\Delta(t_{n+1}) = \exp(\tilde{\mathbf{L}}'\,\Delta t) \,. \tag{47}$$

This allows

$$\tilde{\mathbf{L}}' := \frac{1}{\Delta t} \log(\bar{\mathbf{F}}_\Delta) \tag{48}$$

to be interpreted as the step-averaged deviatoric part of the velocity gradient, i.e. the unique constant second-order tensor whose exact integration over Δt provides the unimodular relative deformation gradient over the time increment.

The unimodular elastic left Cauchy–Green tensor $\bar{\mathbf{B}}_e$ evolves according to Eq. (6). Over the increment, $\mathbf{L}'(t)$ is substituted with its step-average $\tilde{\mathbf{L}}'$ defined in Eq. (48), and $\mathbf{L}_p'$ is computed from the FE DOFs $\Delta\hat{\mathbf{L}}_{pt} = \hat{\mathbf{L}}_{pt}\Delta t$ and $\Delta\hat{\mathbf{L}}_{p33} = \hat{\mathbf{L}}_{p33}\Delta t$ at the end of the time increment as

$$\mathbf{L}_p'\Delta t = \mathcal{I}_d \left\{ \mathcal{E}_t(h_e^{(i)}, \mathbf{v}^{(i)})\Delta\hat{\mathbf{L}}_{pt} + \left[\mathcal{E}_{S\mathcal{K}}^T(h_e^{(i)}, \mathbf{v}^{(i)})\Delta\hat{\mathbf{L}}_{pt}\right]\mathbf{I}_{skw} + \boldsymbol{E}_z\,\Delta\hat{\mathbf{L}}_{p33} \right\},$$

where $\mathbf{I}_{skw} = [0\ \ 0\ \ 0\ \ 1\ \ -1]^T$ and

$$\mathcal{I}_d = \begin{bmatrix} \frac{2}{3} & -\frac{1}{3} & -\frac{1}{3} & 0 & 0 \\ -\frac{1}{3} & \frac{2}{3} & -\frac{1}{3} & 0 & 0 \\ -\frac{1}{3} & -\frac{1}{3} & \frac{2}{3} & 0 & 0 \\ 0 & 0 & 0 & 1 & 0 \\ 0 & 0 & 0 & 0 & 1 \end{bmatrix}$$

denotes the matrix operator corresponding to the fourth-order tensor extracting the deviatoric part of a second-order tensor.

By introducing

$$\mathbf{L}'_e := \tilde{\mathbf{L}}' - \mathbf{L}'_p ,$$

Eq. (6) reduces to a linear differential equation in matrix form with constant coefficients. Its exact incremental solution reads

$$\bar{\mathbf{B}}_{e,n+1} = \exp(\mathbf{L}'_e \Delta t)\, \bar{\mathbf{B}}_{e,n}\, \exp(\mathbf{L}'_e \Delta t)^T .$$

Using $\tilde{\mathbf{L}}' \Delta t = \log(\bar{\mathbf{F}}_\Delta)$, one obtains

$$\exp(\mathbf{L}'_e \Delta t) = \exp\left(\log(\bar{\mathbf{F}}_\Delta) - \mathbf{L}'_p \Delta t\right) =: \bar{\mathbf{F}}_{\Delta e} ,$$

so that the unimodular tensor $\bar{\mathbf{B}}_e$ at the end of the time increment is computed as

$$\bar{\mathbf{B}}_{e,n+1} = \bar{\mathbf{F}}_{\Delta e}\, \bar{\mathbf{B}}_{e,n}\, \bar{\mathbf{F}}^T_{\Delta e} .$$

3.2. Time-integration of the Nye-Kröner-like tensor

The Nye-Kröner-like tensor $\boldsymbol{\alpha}$ is obtained by time-integrating Eqs. (2) and (3). Once $\boldsymbol{\alpha}$ is known, the defect stress $\boldsymbol{\zeta}$ is computed from Eq. (21).

With reference to Eqs. (2) and (3), it is convenient to introduce the rotation tensor $\mathbf{R}$ that solves the initial value problem

$$\begin{cases} \dot{\mathbf{R}}(t) = \boldsymbol{\Omega}(t)\mathbf{R}(t) \\ \mathbf{R}(0) = \mathbf{I} \end{cases} \tag{49}$$

By following the approach proposed by de Souza Neto et al. (2008) to compute the Jaumann rate of the Kirchhoff stress, a *rotated Nye's tensor* $\boldsymbol{\alpha}_R$ is introduced in the form

$$\boldsymbol{\alpha}_R = \mathbf{R}^T \boldsymbol{\alpha} \mathbf{R} . \tag{50}$$

By taking the time derivative of this equation and using Eq. (2), after straightforward algebra manipulation, one obtains

$$\dot{\boldsymbol{\alpha}}_R = \mathbf{R}^T \left(\operatorname{curl} \mathbf{L}_p\right) \mathbf{R} .$$

Then, application of the backward Euler rule yields

$$\boldsymbol{\alpha}_R = \boldsymbol{\alpha}_{R,n} + \Delta t\, \mathbf{R}^T_{n+1} \left(\operatorname{curl} \mathbf{L}_p\right)_{n+1} \mathbf{R}_{n+1} .$$

The rotation tensor $\mathbf{R}_{n+1}$ is computed by numerically integrating the initial value problem (49), as discussed below.

The Nye-Kröner-like tensor at the end of the step is then determined by inverting (50), thus obtaining

$$\boldsymbol{\alpha} = \mathbf{R} \boldsymbol{\alpha}_R \mathbf{R}^T = \mathbf{R}\mathbf{R}^T_n \boldsymbol{\alpha}_n \mathbf{R}_n \mathbf{R}^T + \Delta t\, \mathbf{R}\mathbf{R}^T_{n+1} \left(\operatorname{curl} \mathbf{L}_p\right)_{n+1} \mathbf{R}_{n+1} \mathbf{R}^T = \mathbf{R}_\Delta \boldsymbol{\alpha}_n \mathbf{R}^T_\Delta + \Delta t \left(\operatorname{curl} \mathbf{L}_p\right)_{n+1} , \tag{51}$$

where $\mathbf{R}(t_{n+1}) = \mathbf{R}_{n+1} = \mathbf{R}$ and

$$\mathbf{R}_\Delta = \mathbf{R}\mathbf{R}^T_n . \tag{52}$$

Following de Souza Neto et al. (2008), an approximate solution of Eq. (49) is obtained by applying the *generalized exponential map rule*. Considering a generic time interval $\left[t_n, t_{n+1}\right]$, the algorithm approximates $\mathbf{R}$ as the exact solution that would be obtained at t_{n+1} if $\boldsymbol{\Omega}$ were constant throughout the time interval. For backward Euler time-integration, this value is assumed to be equal to

$$\boldsymbol{\Omega}_{n+1} = \boldsymbol{\Omega}\left(t_{n+1}\right) = \mathbf{W}\left(t_{n+1}\right) - k_\Omega\, \mathbf{W}_p\left(t_{n+1}\right) .$$

By following de Souza Neto et al. (2008),

$$\mathbf{R} = \exp\left(\Delta t\, \boldsymbol{\Omega}_{n+1}\right) \mathbf{R}_n ,$$

so that, Eq. (52) yields

$$\mathbf{R}_\Delta = \exp\left(\Delta t\, \boldsymbol{\Omega}_{n+1}\right) . \tag{53}$$

Note that the adopted time-integration algorithm is incrementally objective, which is a common feature of several numerical schemes in finite-deformation elastoplasticity (de Souza Neto et al., 2008). Moreover, the convergence studies related to the numerical results obtained in Section 4 show the robustness of the proposed algorithm. A strongly objective integration scheme within the present framework is non-trivial and is left for a further specific computational investigation. Also, note that the midpoint rule proposed in de Souza Neto et al. (2008), instead of the backward Euler scheme adopted here, has also been implemented, obtaining almost identical results.

3.3. Specialization to 2D boundary value problems

In the case of 2D boundary value problems, both the plastic and total spin rates can be represented as vectors parallel to the out-of-plane axis. Hence, $\boldsymbol{\Omega}_{n+1}$ is the 2D skew-symmetric tensor

$$\boldsymbol{\Omega}_{n+1} = \Omega_{n+1} \begin{bmatrix} 0 & 1 \\ -1 & 0 \end{bmatrix}, \tag{54}$$

where, for brevity, the indices 12 have been dropped from the scalar Ω_{n+1} and

$$\Omega_{n+1} = W_{12}(t_{n+1}) - k_\Omega\, W_{p12}(t_{n+1})\,. \tag{55}$$

In this case, the tensor exponent in Eq. (53) can be easily computed in the closed form

$$\mathbf{R}_\Delta = \exp\left(\Delta t\, \boldsymbol{\Omega}_{n+1}\right) = \begin{bmatrix} \cos\left(\Omega_{n+1}\Delta t\right) & \sin\left(\Omega_{n+1}\Delta t\right) & 0 \\ -\sin\left(\Omega_{n+1}\Delta t\right) & \cos\left(\Omega_{n+1}\Delta t\right) & 0 \\ 0 & 0 & 1 \end{bmatrix}. \tag{56}$$

Moreover, expressing in array notation the non-vanishing components of $\boldsymbol{\alpha}$ in Eq. (36) as

$$[\boldsymbol{\alpha}] = \begin{bmatrix} 0 & 0 & \alpha_{13} \\ 0 & 0 & \alpha_{23} \\ \alpha_{31} & \alpha_{32} & 0 \end{bmatrix} \rightarrow \boldsymbol{\alpha} = \begin{bmatrix} \alpha_{13} \\ \alpha_{23} \\ \alpha_{31} \\ \alpha_{32} \end{bmatrix} \tag{57}$$

yields

$$\boldsymbol{\alpha} = \mathbf{M}_{R\Delta}\boldsymbol{\alpha}_n + \Delta t \left(\operatorname{curl} \mathbf{L}_p\right)_{n+1}, \tag{58}$$

where

$$\mathbf{M}_{R\Delta} = \begin{bmatrix} \cos\left(\Omega_{n+1}\Delta t\right) & \sin\left(\Omega_{n+1}\Delta t\right) & 0 & 0 \\ -\sin\left(\Omega_{n+1}\Delta t\right) & \cos\left(\Omega_{n+1}\Delta t\right) & 0 & 0 \\ 0 & 0 & \cos\left(\Omega_{n+1}\Delta t\right) & \sin\left(\Omega_{n+1}\Delta t\right) \\ 0 & 0 & -\sin\left(\Omega_{n+1}\Delta t\right) & \cos\left(\Omega_{n+1}\Delta t\right) \end{bmatrix}. \tag{59}$$

Both Ω_{n+1} and $\left(\operatorname{curl} \mathbf{L}_p\right)_{n+1}$ must be computed as functions of the FE DOFs.

The total spin rate is computed as

$$W_{12}(t_{n+1}) = \frac{1}{\Delta t} \mathcal{W}^T(\mathbf{H})\Delta\hat{\mathbf{u}}\,, \tag{60}$$

where $\mathcal{W}(\mathbf{H})$ is a linear function that maps components of $\mathbf{H}$ into the vector

$$\mathcal{W}(\mathbf{H}) = \frac{1}{2}\begin{bmatrix} \mathbf{H}_{21} & -\mathbf{H}_{11} & \mathbf{H}_{22} & -\mathbf{H}_{12} & \mathbf{H}_{23} & -\mathbf{H}_{13} & \mathbf{H}_{24} & -\mathbf{H}_{14} \end{bmatrix}^T. \tag{61}$$

Note that $\operatorname{curl} \mathbf{L}_p$ at the end of the increment is computed by using Eq. (44).

The whole user element (`uel`) subroutine for the FE code Abaqus/Simulia (Dassault Systèmes, 2024) is provided in the Supplementary Material.

4. Results and discussion

All the results presented in this section have been obtained with the FE code Abaqus/Simulia (Dassault Systèmes, 2024), where the FE algorithm provided in Section 3 has been implemented in a user element subroutine (`uel`).

4.1. Cyclic simple shear

The first benchmark problem is the classical simple shear of a constrained strip, as depicted in Fig. 1. The strip has initial height H along the through-the-thickness reference coordinate X_2 and is unbounded along the reference coordinates X_1 and X_3. Material points at $X_2 = 0$ are fully clamped and those at $X_2 = H$ are constrained along the X_2 direction. Plane-strain conditions are assumed, with $X_3 \equiv x_3$ for the out-of-plane axis. At $X_2 = H$, the strip is subjected to a uniform displacement $\bar{u}$ in the X_1 direction, which, by referring to Eq. (25), is applied at the rate

$$\dot{\bar{u}}/H = 3/\mathrm{s}\,, \quad \text{with rate-sensitivity} \quad \dot{\varepsilon}_0 = 10^{-4}\,1/\mathrm{s}\,. \tag{62}$$

The material parameters are selected by referring to copper. The basic conventional parameters

$$\mu = 45.1128\,\mathrm{GPa}\,, \quad k = 117.647\,\mathrm{GPa}\,, \quad S_0 = 68\,\mathrm{MPa} \tag{63}$$

are common to all the analyses presented in the following, for which microhard boundary conditions (BCs) are always adopted, i.e., from Eq. (15),

$$L_{p11}(0) = L_{p11}(H) = 0\,, \quad L_{p21}(0) = L_{p21}(H) = 0\,, \quad L_{p33}(0) = L_{p33}(H) = 0\,. \tag{64}$$

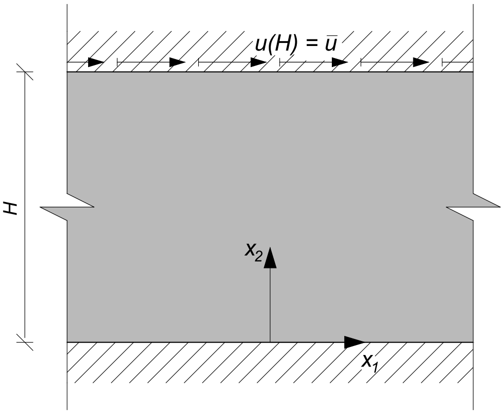

Fig. 1. Schematic of the simple shear problem (from Panteghini et al. (2025a)) with the in-plane reference system (X_1, X_2).

The higher-order BCs on L_{p11} and L_{p33}, clearly, play a role in the finite-deformation context *only*, as L_{p11} and L_{p33} vanish in small-strain simple shear. Under small strains and rotations, microhard BCs would imply that L_{p21} is a parabolic function of X_2 (Panteghini and Bardella, 2018). Within this investigation, results have been obtained by varying the out-of-plane higher-order BC, to be either microhard, or microfree (see Eqs. (16) and (33) and the discussion below about Eq. (36)), i.e.

$$L_{p33,1}(0) = L_{p33,1}(H) = L_{p33,2}(0) = L_{p33,2}(H) = 0\,. \tag{65}$$

If material parameters typical of metals are adopted as in Eq. (63), the force-displacement response of the strip is the same regardless of whether conditions (64) on L_{p33} or (65) are applied. However, numerical tests performed by setting a significantly larger ratio between S_0 and μ than that in Eq. (63), thus allowing much larger elastic deformations to develop, have shown that the gradient experienced by L_{p33} may influence the force-displacement response. In this case, contrary to the results presented in the following, the B_e and the LN models give different responses. This is because the use of different nonlinear elastic strain measures $\mathcal{E}'_e$ yields different out-of-plane responses even in conventional finite-deformation simple shear (Panteghini et al., 2025b). Since the present study focuses on the typical behavior of metals, results for moderate to large elastic deformations are omitted for the sake of brevity. However, on the basis of this discussion, in the following, the terminology “full microhard BCs” is adopted for the application of Eq. (64).

The strip size H is varied to discuss the observed behavior in terms of the ratio

$$r = \frac{H}{\ell}\,, \tag{66}$$

with $r \to \infty$ and $r = 1$ corresponding to size-independent plasticity and to the strongest sample considered, respectively. The responses of both the B_e and LN models are compared for ranges of r and values of the parameter χ controlling the dissipation due to the plastic spin rate. Initially, the isotropic hardening in Eq. (24) is ignored.

The FE mesh consists of a column of 381 FEs with a continuous bias, to have a finer discretization where plastic flow gradients are larger, resulting in a ratio between the central and edge FEs equal to ≈1998. A mesh-sensitivity study (unreported for brevity) has confirmed that further mesh refinement leaves the results basically unaltered. Also, nodes having the same X_2 are relatively constrained such that results are independent of X_1.

4.1.1. Discussion of the higher-order governing equations

The results in Eq. (36) for the structure of the Nye-Kröner-like tensor under plane-strain conditions can be conveniently discussed for the simple shear problem by neglecting, in Eq. (36), $\partial()/\partial x_1$ and the through-the-thickness velocity, thus obtaining

$$\begin{bmatrix} 0 & 0 & \frac{\partial \alpha_{13}}{\partial t} \\ 0 & 0 & \frac{\partial \alpha_{23}}{\partial t} \\ \frac{\partial \alpha_{31}}{\partial t} & \frac{\partial \alpha_{32}}{\partial t} & 0 \end{bmatrix} \approx \begin{bmatrix} 0 & 0 & \Omega_{12}\alpha_{23} \\ 0 & 0 & -\Omega_{12}\alpha_{13} \\ \Omega_{12}\alpha_{32} & -\Omega_{12}\alpha_{31} & 0 \end{bmatrix} + \begin{bmatrix} 0 & 0 & -L_{p11,2} \\ 0 & 0 & -L_{p21,2} \\ L_{p33,2} & 0 & 0 \end{bmatrix}. \tag{67}$$

Note that under small strains and rotations the sole non-vanishing evolution equation for $\boldsymbol{\alpha}$ reads $\dot{\alpha}_{23} \equiv \partial\alpha_{23}/\partial t = -L_{p21,2}$, such that non-vanishing α_{13}, α_{31}, and α_{32} are due to the finite-deformation formulation.

In the linear theory (Gurtin, 2004), the sole non-vanishing components of $\boldsymbol{\alpha}$ and $\mathbf{M}$ are α_{23} and $M_{12} \equiv T_{12}$, and the sole non-vanishing spatial derivative is that with respect to $X_2 \equiv x_2$, such that the higher-order balance Eqs. (38) and (39) reduce to

$$\begin{aligned} &\chi S V(d_p)\frac{W_{p12}}{d_p} = \frac{\mu\ell^2}{2}\alpha_{23,2} \equiv \frac{\mu\ell^2}{2}\int_t (W_{p12} - D_{p12})_{,22}\,\mathrm{d}t\,, \\ &\mu\left(u_{1,2} - 2\int_t D_{p12}\,\mathrm{d}t\right) \equiv T_{12} = \frac{2}{3}SV(d_p)\frac{D_{p12}}{d_p} + \frac{\mu\ell^2}{2}\alpha_{23,2} \equiv \frac{2}{3}SV(d_p)\frac{D_{p12}}{d_p} + \frac{\mu\ell^2}{2}\int_t (W_{p12} - D_{p12})_{,22}\,\mathrm{d}t\,. \end{aligned} \tag{68}$$

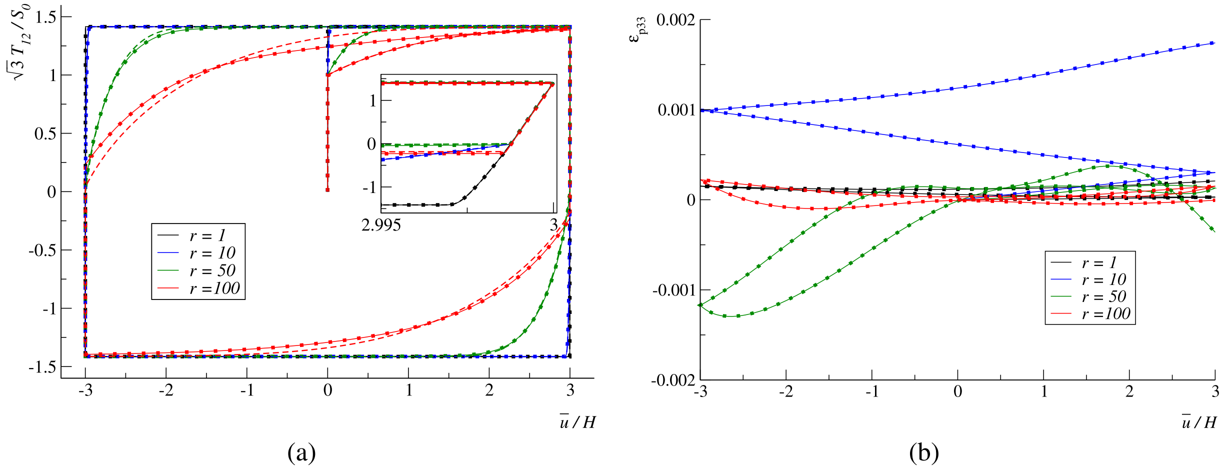

Fig. 2. Non-dimensional Cauchy shear stress (a) and current out-of-plane plastic strain, defined as in Eq. (70), at $X_2 = H/2$ (b) as a function of the non-dimensional applied shear displacement for perfect plasticity under full microhard BCs, with $\chi = 2/3$ and $k_\Omega = 0$. Continuous, dotted, and dashed curves refer to the B_e, LN, and small-strain models, respectively.

With reference to Eq. (37), the most important higher-order balance equations for finite-deformation simple shear are those involving the components $(\mathrm{curl}\,\boldsymbol{\zeta})\cdot(\mathbf{e}_1\otimes\mathbf{e}_1)$ and $(\mathrm{curl}\,\boldsymbol{\zeta})\cdot(\mathbf{e}_2\otimes\mathbf{e}_1)$. These equations are obtained from specialization of the relations in Eq. (39) as

$$\frac{2\mu\ell^2}{3}\Big(\frac{\alpha_{13}}{J}\Big)_{,2} = T'_{11} - \frac{2}{3}SV(d_p)\frac{D_{p11}}{d_p}\,, \quad \frac{\mu\ell^2}{3}\Big(\frac{\alpha_{13}}{J}\Big)_{,2} = \frac{2}{3}SV(d_p)\frac{D_{p22}}{d_p} - T'_{22}\,, \quad \frac{\mu\ell^2}{3}\Big(\frac{\alpha_{13}}{J}\Big)_{,2} = \frac{2}{3}SV(d_p)\frac{D_{p33}}{d_p} - T'_{33}\,,$$
$$\frac{1}{2}\mu\ell^2\Big(\frac{\alpha_{23}}{J}\Big)_{,2} = T_{12} - \frac{2}{3}SV(d_p)\frac{D_{p12}}{d_p}\,, \quad \frac{1}{2}\mu\ell^2\Big(\frac{\alpha_{23}}{J}\Big)_{,2} = \chi SV(d_p)\frac{W_{p12}}{d_p}\,, \tag{69}$$

where the last two relations are the finite-deformation counterparts of those in Eq. (68). Note that the relevance of the first three relations depends on the coupling between α_{23} and α_{13} in Eq. (67), that is, from the value assumed by Ω_{12} within the loading history. Specifically, the third relation in Eq. (69) implies that, irrespective of the form of T'_{33}, which is different in the B_e and LN models, an out-of-plane plastic strain rate arises due to α_{13} that, in turn, develops because of the presence of α_{23}. Hence, full microhard BCs surely yields a non-vanishing $L_{p33,22}$.

4.1.2. Results and discussion

The results are presented by beginning with those obtained by setting $k_\Omega = 0$ in Eq. (3), which follows the proposal in (Rubin and Bardella, 2023).

Fig. 2 studies the size-dependent cyclic response by varying the ratio r, as defined in Eq. (66). As a partial verification of the FE code, the response under monotonic loading for the small-strain case has been compared with the analytical solution obtained in Panteghini and Bardella (2018), which holds in the absence of hardening and is exact in the rate-independent case. Specifically, Fig. 2 focuses on very large deformations, as the applied shearing displacement cycles in the range $[-3H, 3H]$, and illustrates the results in terms of the Cauchy shear stress normalized with respect to the initial yield shear stress $S_0/\sqrt{3}$ and in terms of the out-of-plane plastic strain, defined as

$$\varepsilon_{p33} = \int_0^t L_{p33}(\tau)\mathrm{d}\tau\,, \tag{70}$$

which, in Fig. 2(b), is evaluated in the middle of the strip, i.e. where it is maximum. It is important to note that, here and henceforth, T_{12} is actually the average value evaluated from the reaction forces related to the degrees of freedom used to apply the shearing displacement $\bar{u}$; of course, such an average is pointwise exact for small strains and rotations, while for finite deformations its closeness to any local value depends on r. In the following figures, as indicated in the captions, other variables that are functions of x_2, are evaluated at $x_2 = H/2$ when plotted against $\bar{u}$ (note that if $x_2 = H/2$ one also has $x_2 = X_2$ because $u_2(x_2 = H/2) = 0$).

The results can be interpreted by resorting to the analytical solution for small-strain perfect plasticity (i.e. $S = S_0$ and $V(d_p) = 1$ are constants, Panteghini and Bardella (2018)). An outcome of this solution is that in simple shear the maximum possible value of the equivalent effective Cauchy stress $\sqrt{3\mathbf{T}'\cdot\mathbf{T}'/2}$ is $S_0\sqrt{1+3\chi/2}$, such that the saturated value of the Cauchy shear stress is

$$T_{12}^{\mathrm{sat}} = \frac{S_0}{\sqrt{3}}\sqrt{1+\frac{3\chi}{2}}\,, \tag{71}$$

which depends only on the initial yield stress S_0 and the parameter χ governing the dissipation due to the plastic spin rate. Even for finite deformations, this is the maximum shear stress value reached for all the strip sizes, as displayed in Fig. 2(a) for the case

$\chi = 2/3$. This result also implies that the rate-sensitivity parameter $\dot{\epsilon}_0$ as selected in Eq. (62) is small enough to obtain solutions that share important features with the case of rate-independent plasticity.

In this work, the analytical solution for small-strain perfect plasticity is extended to predict the strip behavior when resuming plasticity after loading inversion. By using the results in Panteghini and Bardella (2018) and assuming that the saturation stress in Eq. (71) has been reached under monotonic loading, the higher-order balance Eq. (68) become

$$\chi S_0 \frac{W_{p12}}{d_p} = \frac{\frac{3\chi}{2}}{\sqrt{1+\frac{3\chi}{2}}} \frac{S_0}{\sqrt{3}},$$
$$T_{12} = \frac{2}{3} S_0 \frac{D_{p12}}{d_p} + \frac{\frac{3\chi}{2}}{\sqrt{1+\frac{3\chi}{2}}} \frac{S_0}{\sqrt{3}}, \tag{72}$$

where

$$d_p = \sqrt{\frac{4}{3} D_{p12}^2 + 2\chi W_{p12}^2} \tag{73}$$

and one has

$$D_{p12} = W_{p12}\,, \quad \text{such that} \quad L_{p21} = 0 \quad \text{and} \quad L_{p12} \text{ is spatially uniform}\,,$$

corresponding to the impossibility for the defect stress to further increase.

After loading reversal, the contribution due to the defect stress at the right-hand sides of the two balance equations in (72) may not change, as it depends on the accumulated plasticity only; these higher-order balance equations, however, may not be used until plasticity resumes. When this happens, the first relation in Eq. (72) provides

$${d_p}^2 = \frac{4}{3}\left(1 + \frac{3\chi}{2}\right) W_{p12}^2\,, \tag{74}$$

which can be substituted in Eq. (73) to obtain

$$|D_{p12}| = |W_{p12}|\,,$$

still holding at the instant when plasticity resumes. Specifically, because of the first relation in Eq. (72), W_{p12} at incipient plasticity upon loading reversal is identical to W_{p12} when the saturation stress in Eq. (71) is reached under monotonic loading. Instead, D_{p12} must change sign when plasticity resumes, so that one has

$$D_{p12} = -W_{p12}\,, \quad \text{such that} \quad L_{p12} = 0 \quad \text{and plasticity due to } L_{p21} \text{ is initially recovered}\,, \tag{75}$$

thus decreasing the defect stress.

Finally, by substituting the results in Eqs. (74) and (75) into the second higher-order balance equation in Eq. (72) one obtains

$$T_{12}^{\text{res}} = \frac{\frac{3\chi}{2} - 1}{\sqrt{1+\frac{3\chi}{2}}} \frac{S_0}{\sqrt{3}}, \tag{76}$$

which is the analytical expression for the value of the Cauchy shear stress at the onset of plasticity after loading reversal, upon stress saturation has been reached under monotonic loading (with $T_{12} > 0$). Eq. (76) establishes that $\chi \in [0, 2/3)$ allows T_{12}^{res} to change sign before plasticity resumes.[4] Specifically, for the case $\chi = 2/3$ in Fig. 2, $T_{12}^{\text{res}} = 0$, which agrees well with the obtained numerical results, as visible in the detail of Fig. 2(a), where note that $T_{12}^{\text{res}} \neq 0$ for $r = 100$ because in this case T_{12} has not reached T_{12}^{sat} in the first loading ramp. More results that can be explained by resorting to the foregoing analytical solution will be discussed later when introducing isotropic hardening.

Several other conclusions can be drawn on the basis of the results in Fig. 2. The first one is that the B_e and LN models provide almost identical results; this is because of the limited influence of elastic deformation in metals' elastoplasticity. The response of these two finite-deformation models is remarkably close to the small-strain response for what concerns the Cauchy shear stress (Fig. 2(a)) even in the transition between the initial yielding and T_{12}^{sat}. The largest discrepancy is visible for the case $r = 50$, and it is due to a finite-deformation effect. In fact, it is important to note that the difference between the finite-deformation and small-strain results in terms of T_{12} is not due to the gradient experienced by L_{p33}, i.e. by α_{31} and α_{32}, which is absent in the small-strain case. This is known because almost identical results have been obtained regardless of whether the out-of-plane BCs are microhard (as in Eq. (64)) or microfree (see Eq. (65)). Of course, the out-of-plane plastic strain in Fig. 2(b) characterizes the finite-deformation responses only, being identically zero in the small-strain case. Again, these results for $\epsilon_{p33}(x_2 = H/2)$ show perfect agreement between the B_e and LN models. With reference to Eq. (69) and the discussion following it, this agreement means that the presence of non-vanishing L_{p33} has to be ascribed to the same α_{23} profile predicted by the two models. Even more interestingly, Fig. 2(b) suggests a complex nonlinear

[4] It is recalled that in the case $\chi = 0$ there is no dissipation associated to the plastic spin rate and Eq. (38) suggests that W_{p12} tends to assume a profile minimizing the defect energy. Specifically, in the small-strain case W_{p12} is equal to D_{p12} so that L_{p21} vanishes and one recovers conventional plasticity (Panteghini and Bardella, 2018).

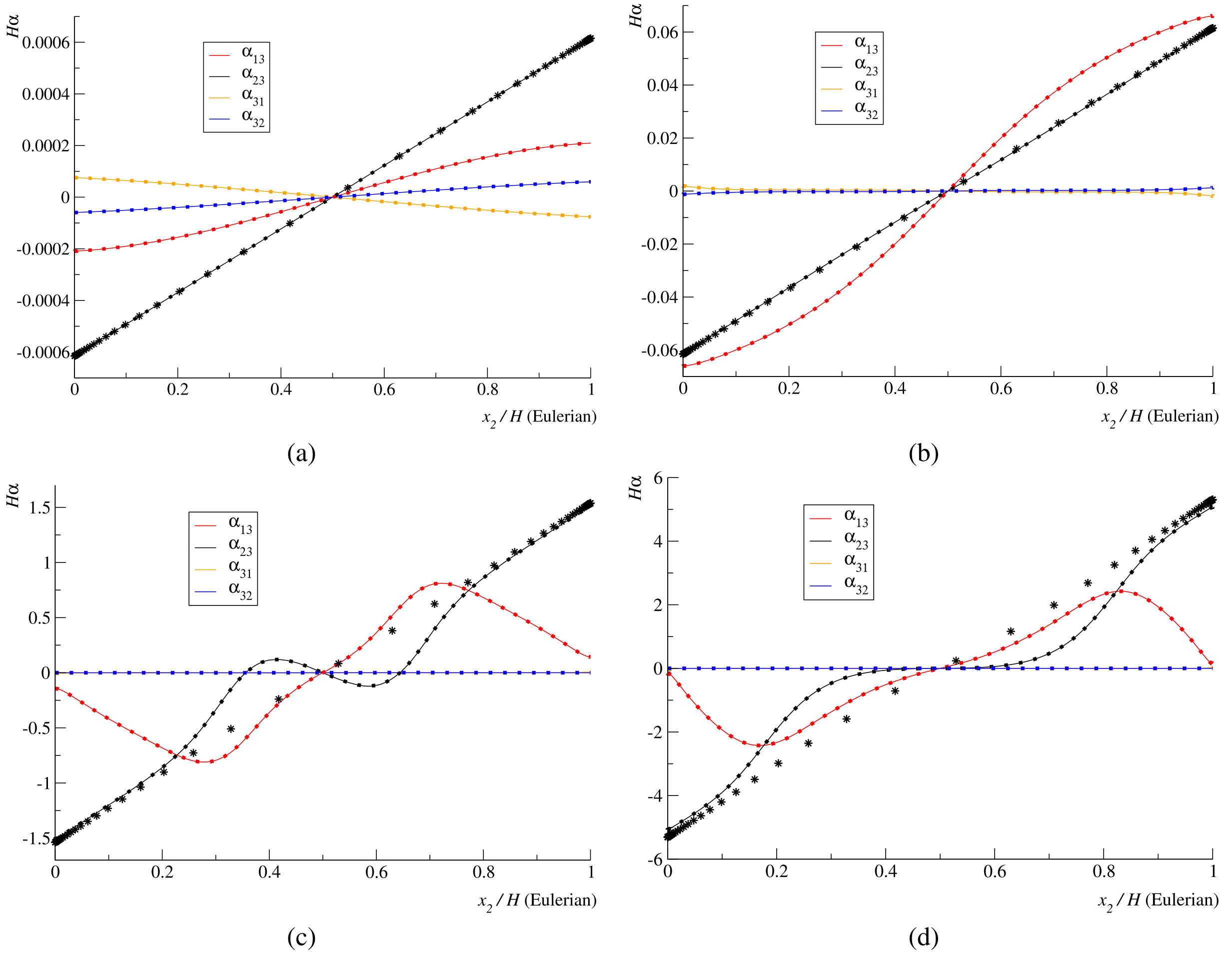

Fig. 3. Monotonic simple shear with $\chi = 2/3$, $k_\Omega = 0$, and full microhard BCs. Non-dimensional components of the Nye-Kröner-like tensor at applied shearing displacement $\bar{u}/H = 3$ for four sample sizes: $r = 1$ (a), $r = 10$ (b), $r = 50$ (c), $r = 100$ (d). Continuous, dotted, and star curves refer to the B_e, LN, and small-strain models, respectively.

behavior, where the responses in terms of ε_{p33} cannot be monotonically ordered with respect to r. This is due to the large deformations and, more specifically, to the large spin rates that couple the evolution equations for the components of $\boldsymbol{\alpha}$ (Eq. (67)). As illustrated in the following, this holds also for other local fields.

In fact, this clearly emerges from inspection of Fig. 3, showing the non-dimensional profiles of the Nye-Kröner-like tensor components at the end of a large-deformation monotonic loading ramp, with $\bar{u}/H = 3$, for four different strip sizes. Again, it is observed that the B_e and LN models give almost coincident results. The contributions of α_{31} and α_{32}, which identically vanish for small strains and rotations, are almost negligible. The maximum magnitude of α_{23} is proportional to ℓ^2 and this holds for the whole profile of α_{23} in the range $r \in [1, 10]$. This suggests that the curl of the defect stress associated to α_{23} is independent of the size r for such a large applied displacement, for which the shear stress has basically reached its saturation value. For the sizes corresponding to $r = 1$ and $r = 10$ (Fig. 3 (a) and (b), respectively), the finite-deformation prediction of α_{23} is almost coincident with the straight line obtained from the small-strain theory. Instead, for $r = 50$ and $r = 100$ (Fig. 3 (c) and (d), respectively) the coupling between α_{13} and α_{23} in the evolution equation for $\boldsymbol{\alpha}$ (see Eq. (67)) yields a nonlinear profile for α_{23}. Additionally, for the case $r = 10$, illustrated in Fig. 3(b), it is observed that the component α_{13} has about the same magnitude as α_{23}. This behavioral feature depends on the evolution equation for $\boldsymbol{\alpha}$, as will be confirmed later when discussing the influence of k_Ω on the results.

Fig. 4 shows the profiles, along the strip height, of the displacement components, u_1 and u_2, the latter being zero in the small-strain case. These profiles refer to the end of a monotonic loading ramp with $\bar{u} = 3H$. For the two sizes corresponding to $r = 10$ and $r = 50$ the finite-deformation response in terms of u_1, again basically the same for the B_e and LN models, is significantly different from the small-strain response, although the same stress T_{12}^{sat} is reached in all cases, as clear from Fig. 2. The α_{13} profiles shown in Fig. 3 constitute one of the factors contributing to this difference. Additionally, Fig. 4(b) shows that the through-the-thickness displacement component remains small, as expected, in the finite-deformation models, but it exhibits a non-monotonic behavior, with respect to r, of the maximum value it attains along the strip height.

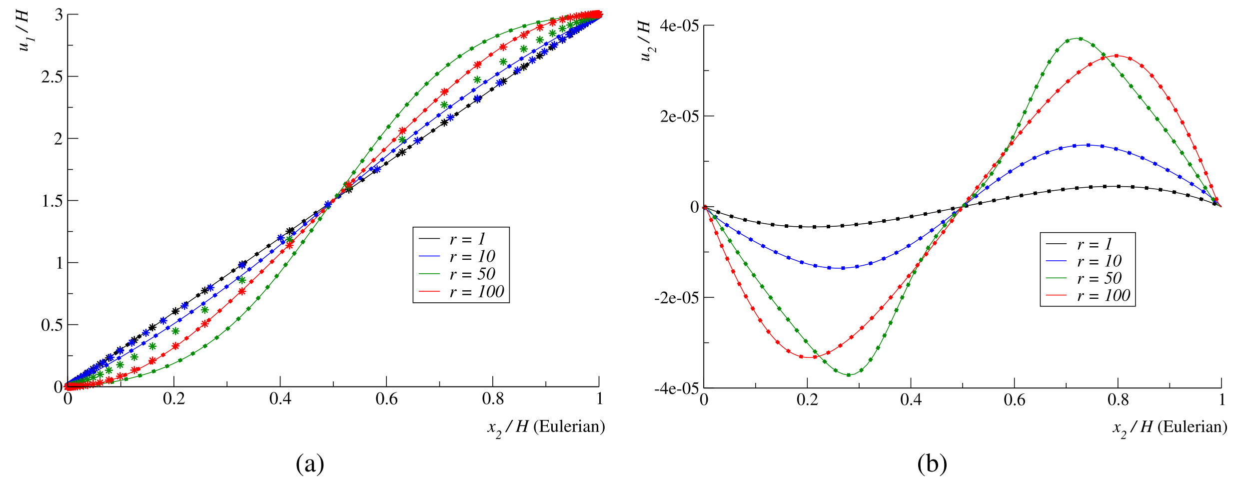

Fig. 4. Monotonic simple shear with $\chi = 2/3$, $k_\Omega = 0$, and full microhard BCs. Non-dimensional displacement components u_1/H (a) and u_2/H (b) at applied shearing displacement $\bar{u}/H = 3$. Continuous, dashed, and star curves refer to the B_e, LN, and small-strain models, respectively. Note that in figure (b) small-strain results are not displayed as $u_2 = 0\ \forall r$ in that case.

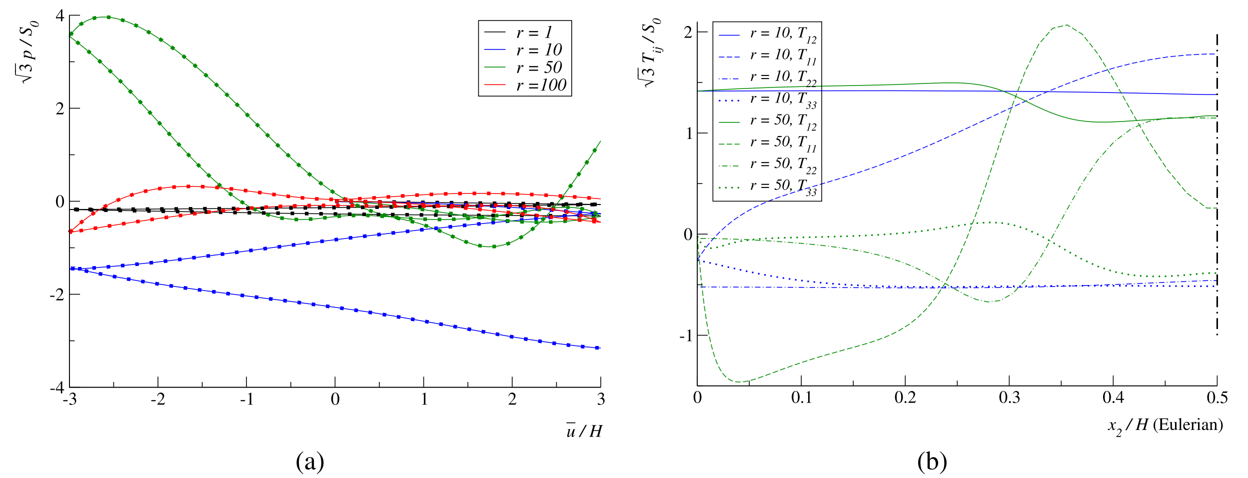

Fig. 5. Simple shear with $\chi = 2/3$, $k_\Omega = 0$, and full microhard BCs. Non-dimensional pressure, at $X_2 = H/2$, under cyclic loading (a); continuous and dashed curves refer to the B_e and the LN models, respectively. Non-dimensional Cauchy stress components after monotonic loading up to $\bar{u}/H = 3$ (b); B_e model only (for the sake of graphical clarity).

Fig. 5 further highlights the effect of finite deformations on the simple shear response by showing the pressure evolution under cyclic loading and the Cauchy stress components after the first loading ramp, with $\bar{u}/H = 3$. Note that the pressure is defined, in Eq. (18), as positive if compressive; hence, from the comparison between Figs. 5(a) and 2(b) one observes that the pressure does not necessarily have a sign directly implied by that of the out-of-plane Cauchy stress, the latter having sign opposite to that of the out-of-plane plastic strain. In fact, either of the in-plane direct stress components can be significantly larger than the out-of-plane stress. Interestingly, Fig. 5(b) shows that the shear stress is not necessarily larger than the largest of the in-plane direct stress components. Note that, for the sake of clarity, Fig. 5(b) exploits the Cauchy stress symmetry with respect to $X_2 = H/2$, thus plotting the results only for $x_2/H \in [0, 0.5]$. Fig. 5(a) confirms previous conclusions that certain results may not be ordered monotonically with r and that the B_e and LN models provide almost identical results for the adopted set of material parameters, leading to relatively small elastic deformations.

Some details of the behavior discussed so far are due to the choice of k_Ω in the evolution equation for $\boldsymbol{\alpha}$ (see Eq. (67)), as is clear from Fig. 6, which shows differences in the predictions for $k_\Omega = 0$ and $k_\Omega = 1$ for the B_e model only (given that the LN model provides basically the same results, as illustrated so far). The main result is that the finite-deformation predictions for $k_\Omega = 1$ are significantly closer to the small-strain predictions, and this is further illustrated in Fig. 7, showing the comparison in terms of the Nye-Kröner-like tensor components.

The reason for this is that in the case $k_\Omega = 1$ the spin rate Ω_{12} tends to vanish, because the plastic spin rate tends to the total spin rate, such that there is no coupling between α_{23} and α_{13} in Eq. (67), the latter becoming negligible. This is documented in

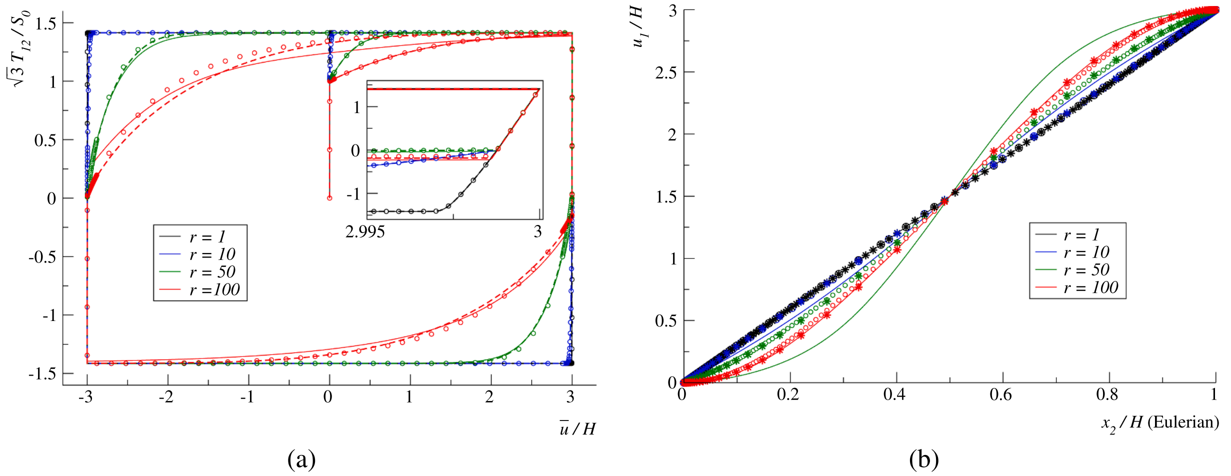

Fig. 6. Cyclic simple shear with $\chi = 2/3$ and full microhard BCs. Non-dimensional Cauchy shear stress (a) and non-dimensional displacement u_1/H at the end of the first loading ramp (i.e., for $\bar{u}/H = 3$) (b). Continuous curves refer to the B_e model with $k_\Omega = 0$; circles refer to the B_e model with $k_\Omega = 1$; dashed curves (a) or stars (b) refer to the small-strain model.

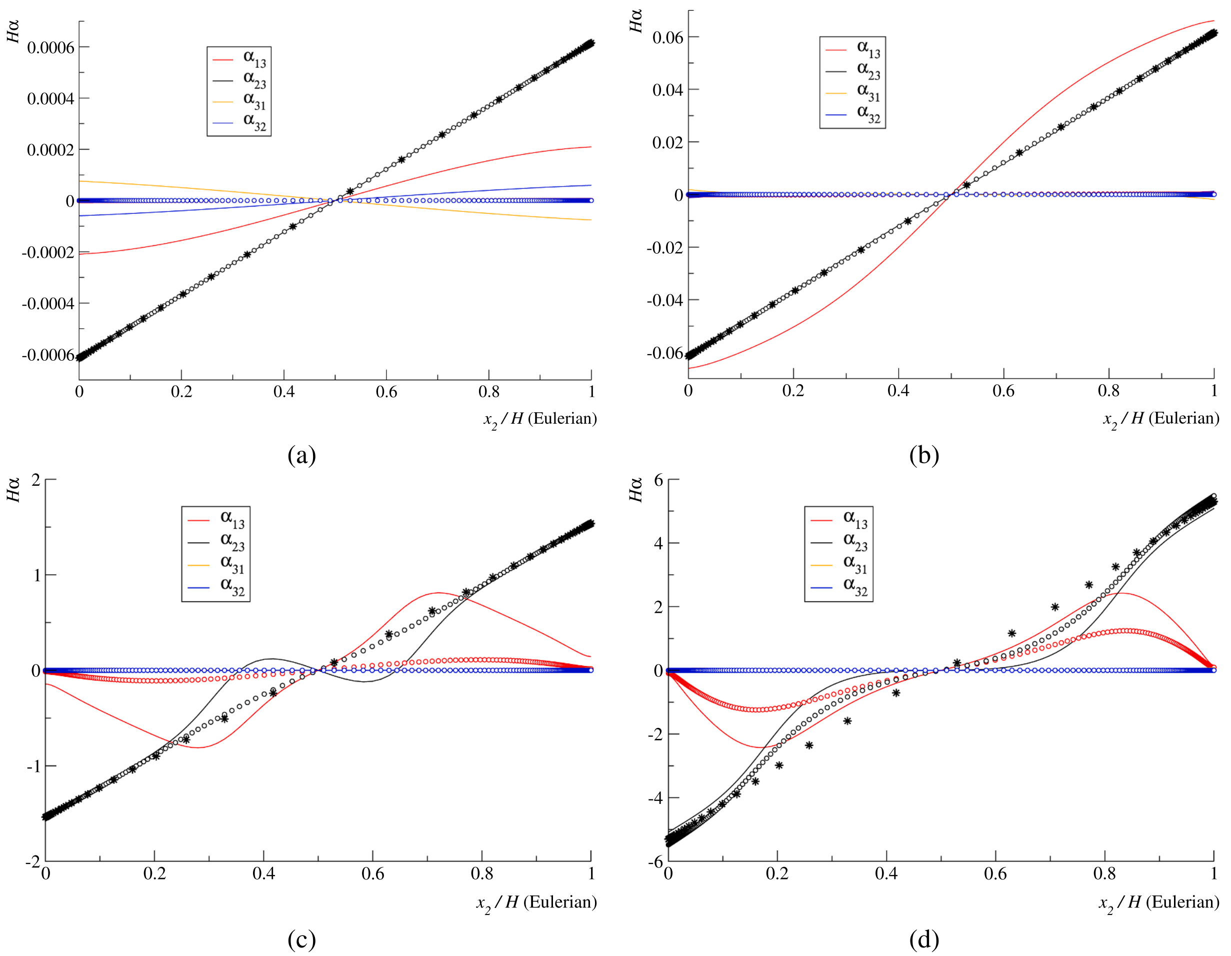

Fig. 7. Monotonic simple shear with $\chi = 2/3$ and full microhard BCs. Non-dimensional components of the Nye-Kröner-like tensor at applied shearing displacement $\bar{u}/H = 3$, for four sample sizes: $r = 1$ (a), $r = 10$ (b), $r = 50$ (c), $r = 100$ (d). Continuous curves refer to the B_e model with $k_\Omega = 0$; circles refer to the B_e model with $k_\Omega = 1$; stars refer to the small-strain model.

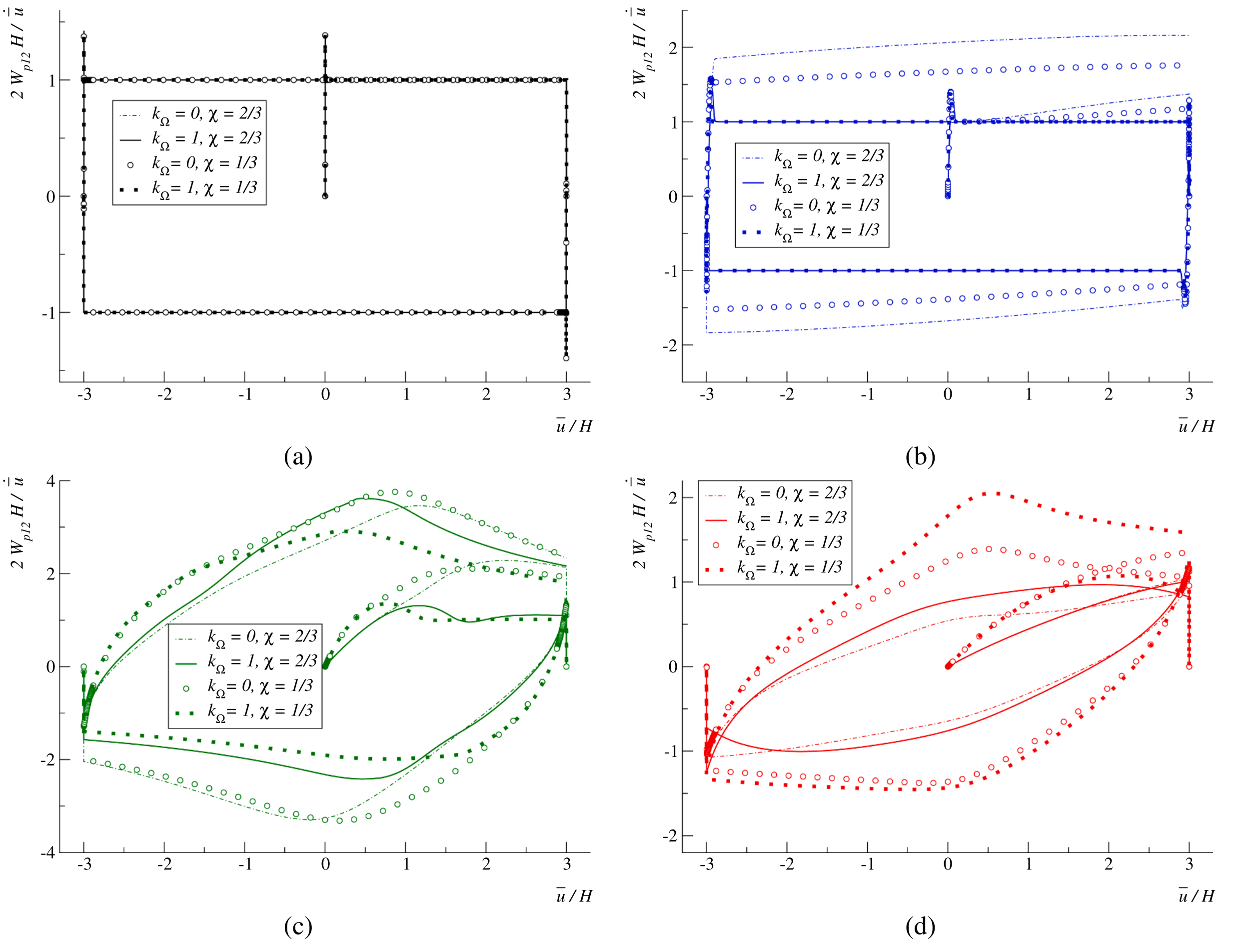

Fig. 8. Influence of k_Ω in cyclic simple shear: non-dimensional W_{p12} at $X_2 = H/2$ for the B$_e$ model and χ = either 2/3 or 1/3. $r = 1$ (a), $r = 10$ (b), $r = 50$ (c), $r = 100$ (d).

Figs. 8 and 9, showing the cyclic behavior of $W_{p12}(X_2 = H/2)$ and $\Omega_{12}(X_2 = H/2)$, respectively, for two values of χ (2/3 and 1/3) and the four sizes considered so far (r =1, 10, 50, 100). Note that Fig. 8 plots $2W_{p12}(X_2 = H/2)H/\dot{\bar{u}}$, which is equal to 1 when W_{p12} is equal to the average total spin rate. The tendency of Ω_{12} to vanish is inversely proportional to r. So, for $k_\Omega = 1$, the stronger the sample, the closer the behavior is to that under small strains and rotations.

The cyclic behavior of W_{p12} is further analyzed in Fig. 10. The response is essentially rate-independent except for the rate-dependent elastic-plastic transition introduced with Eqs. (23) and (25). In this analysis the strain-rate sensitivity parameter is set

$$\dot{\epsilon}_0 = 10^{-9}\,1/\mathrm{s}\,,$$

i.e. much smaller than that adopted so far (see Eq. (62)). Importantly, despite the finite-deformation model, the behavior described in Eq. (75) is almost fully followed here as well. In particular, the detail of Fig. 10 shows that when unloading $D_{p12} = W_{p12} = 0$ and when plasticity resumes, at the stress T_{12}^{res} predicted by Eq. (76), W_{p12} attains the same value as that reached before unloading, whereas $D_{p12} = -W_{p12}$; in fact, the saturation stress T_{12}^{sat} in Eq. (71) is closely approached during loading. Note that the results in the insert of Fig. 10 are slightly affected by the viscoplastic regularization, and this is the reason for adopting a very small value for $\dot{\epsilon}_0$ in this analysis.

With reference to Eq. (24), the results presented in the following for the simple shear benchmark problem involve the isotropic hardening

$$S(\bar{\epsilon}_p) = S_0 + (S_{\mathrm{sat}} - S_0)\tanh\left(a_h\,\bar{\epsilon}_p\right), \tag{77}$$

where a_h governs the rate at which the stress S saturates at S_{sat}. So, the material parameters are still those in Eq. (63), with the addition of

$$S_{\mathrm{sat}} = 139\,\mathrm{MPa}\,, \quad a_h = 9.5\,. \tag{78}$$

These values have been taken from a DGP model, still relying on Gurtin (2004), which has been calibrated in Panteghini and Bardella (2020) to predict the experimental results on the cyclic torsion of thin copper wires obtained by Liu et al. (2013) .

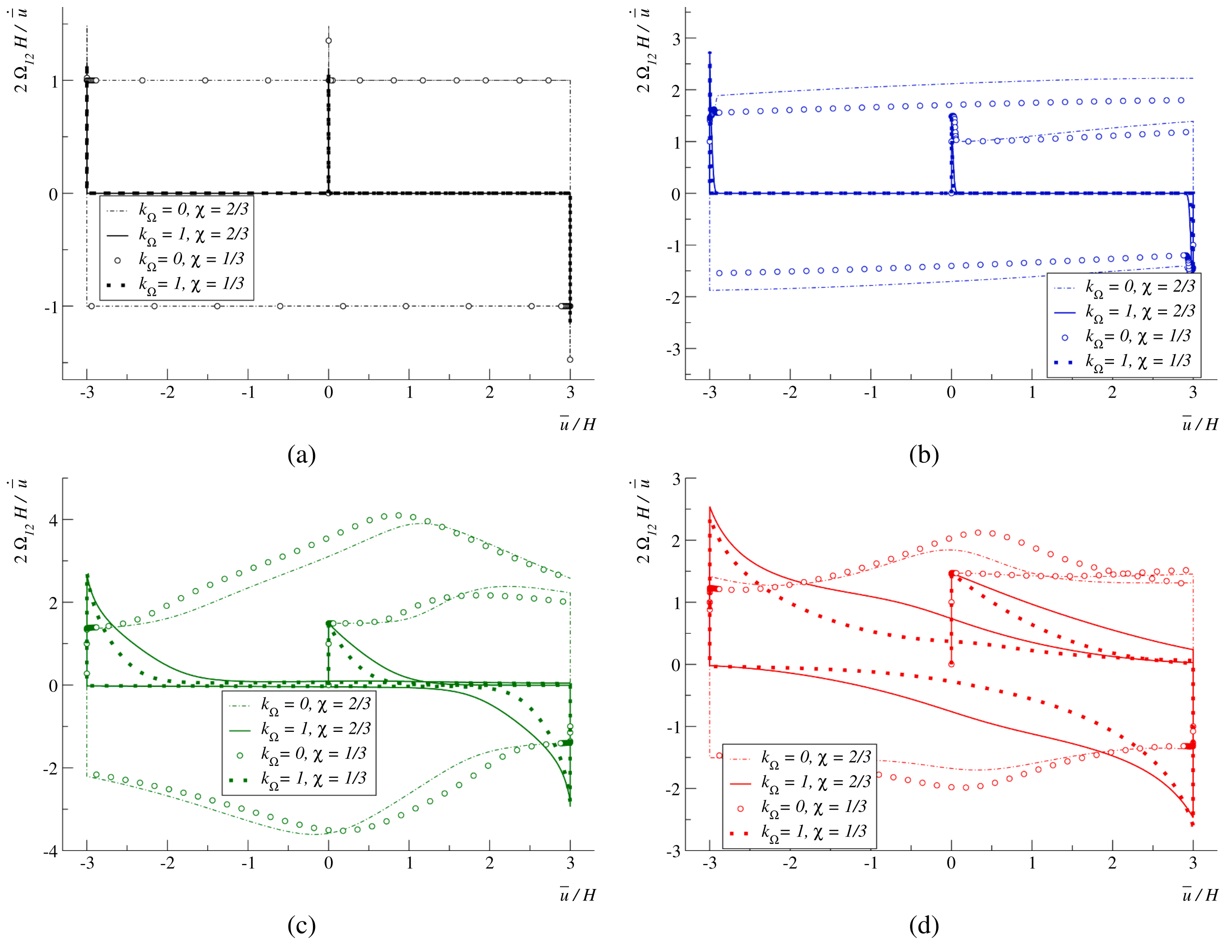

Fig. 9. Influence of k_Ω in cyclic simple shear: non-dimensional Ω_{12} at $X_2 = H/2$ for the B$_e$ model and χ = either 2/3 or 1/3. $r = 1$ (a), $r = 10$ (b), $r = 50$ (c), $r = 100$ (d).

Fig. 11 displays results for the B$_e$, LN, and small-strain models with $k_\Omega = 1$ and $\chi = 2/3$. First of all, it is observed that the finite-deformation models still provide basically coincident responses in terms of the Cauchy shear stress as a function of the applied shearing displacement, even if the isotropic hardening allows for larger elastic deformations with respect to the previous analysis restricted to perfect plasticity.

Interestingly, Eq. (71) for $T_{12}^{\rm sat}$ and (76) for $T_{12}^{\rm res}$ still provide excellent estimates for the saturation stress under monotonic loading and even for the stress at the onset of plasticity after reverse loading, if in those equations S_0 is simply substituted with $S_{\rm sat}$. This is interesting because the analytical solutions in Eqs. (71) and (76) are obtained under the assumption of perfect plasticity (beside small strains and rate-independence, all missing conditions in the present B$_e$ and LN models).

With the parameters in Eqs. (63) and (78), $S_{\rm sat}/S_0 \approx 2.04$ and, having set $\chi = 2/3$, $(S_{\rm sat}/S_0)\sqrt{1+3\chi/2} \approx 2.89$, which corresponds to the maximum shear stress in Fig. (63). For what concerns $T_{12}^{\rm res}$, Eq. (76) provides vanishing shear stress, which is confirmed by the insert in Fig. 11 for the strips whose size has allowed saturation under monotonic loading, i.e. $r = 1$ and $r = 10$.

Fig. 12 refers to $\chi = 1/3$, aiming to further investigate the estimate in Eq. (76) for $T_{12}^{\rm res}$. In this case, Eq. (76) predicts non-vanishing $T_{12}^{\rm res}$, such that it is interesting to consider both perfect plasticity (continuous lines) and saturating isotropic hardening (dashed lines) to check whether it is true that $T_{12}^{\rm res}$ can be predicted by using Eq. (76) in which S_0 is substituted with $S_{\rm sat}$. Hence, for the sake of graphical clarity, Fig. 12 focuses on the B$_e$ model and on $r = 10$ and $r = 50$ only.

The first check is, however, on $T_{12}^{\rm sat}$. The agreement between Eq. (71) with $S_{\rm sat}$ instead of S_0 is remarkable, given that $(S_{\rm sat}/S_0)\sqrt{1+3\chi/2} \approx 2.50$. Then, the function of χ multiplying $S_0/\sqrt{3}$ in Eq. (76) results equal to $-1/\sqrt{6} \approx -0.408$, which finds correspondence on the value of $T_{12}^{\rm res}$ in the detailed insert in Fig. 12 for the case of perfect plasticity. By multiplying this coefficient by the factor $S_{\rm sat}/S_0 \approx 2.04$ one obtains ≈ -0.833, which agrees well with the insert in Fig. 12 for the case of isotropic hardening.

About the size effect under monotonic loading, it is emphasized that Gurtin's DGP theory allows its tuning through the χ parameter. Specifically, the demonstrated validity of Eq. (71) allows one to infer that, by setting $\chi = 0$, Gurtin's DGP predicts vanishing size effect even in finite-deformation simple shear. This tuning of the size effect is useful for certain materials under specific boundary conditions. For instance, the experimental results of Mu et al. (2016) show cases of limited strengthening in simple shear.

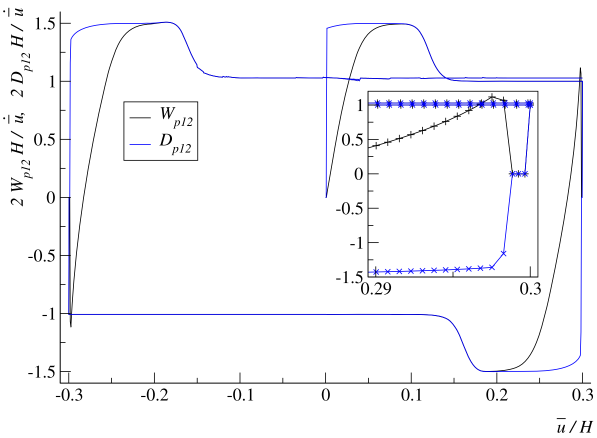

Fig. 10. Non-dimensional W_{p12} and D_{p12} at $X_2 = H/2$: behavior under cyclic loading with the detail about resuming plasticity after the first unloading for the B_e model with $k_\Omega = 1$, $\chi = 2/3$, $r = 10$, $\dot{\epsilon}_0 = 10^{-9}$ 1/s, $\dot{\bar{u}}/H = 0.3$ 1/s.

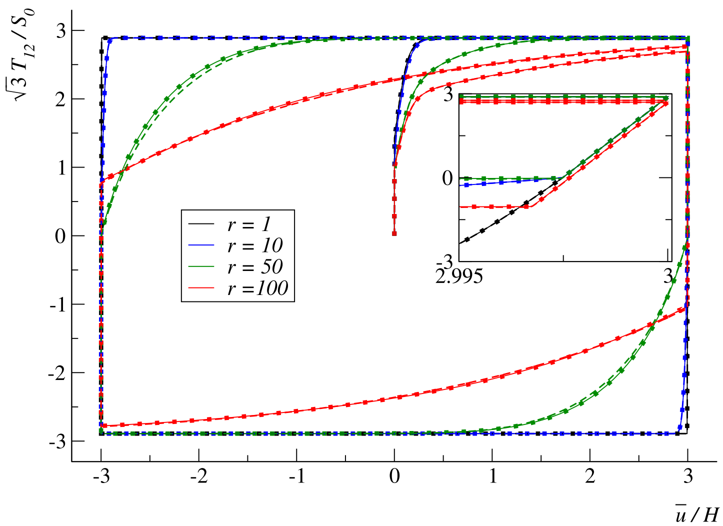

Fig. 11. Cyclic simple shear with full microhard BCs: non-dimensional Cauchy shear stress as a function of the non-dimensional applied shear displacement for the saturating isotropic hardening in Eq. (77), $\chi = 2/3$, and $k_\Omega = 1$. Continuous, dotted, and dashed curves refer to the B_e, LN, and small-strain models, respectively.

Finally, it is remarked that the similarity of the macroscopic response (i.e., average Cauchy shear stress vs applied shearing displacement) predicted by small-strain and finite-deformation theories is lost if larger elastic deformations are allowed, by selecting materials with a smaller ratio between μ and S_0 than that in Eq. (63). While this is omitted in this work for the sake of brevity, the parameters in Eq. (63) here adopted, beside being typical of copper, allow verification of the developed FE code.

4.2. Necking of a plane-strain bar under tension

This benchmark problem is inspired by the classical one of Simo and Armero (1992), which has also been studied by de Souza Neto et al. (2008) and, more recently, in Panteghini et al. (2025b). The main difference between the original problem and that discussed below lies in the axial symmetry of the former, against the plane-strain conditions assumed here.

The geometry of the problem is reported in Fig. 13. The bar has initial length $2H = 53.34$ mm and initial maximum width $B' = 6.413$ mm at the bar edge where the tensile displacement is applied. The initial width is linearly decreased toward the bar center where it reaches the minimum value $B = 6.35$ mm.

A total tensile displacement $\bar{u} = 10$ mm is applied at the rate

$$\dot{\bar{u}} = 1\ \mathrm{mm/s}\,, \quad \text{with rate-sensitivity} \quad \dot{\epsilon}_0 = 10^{-4}\ 1/\mathrm{s}\,,$$

governing the viscoplastic regularization in Eq. (25), whereas the higher-order boundary conditions are microfree.

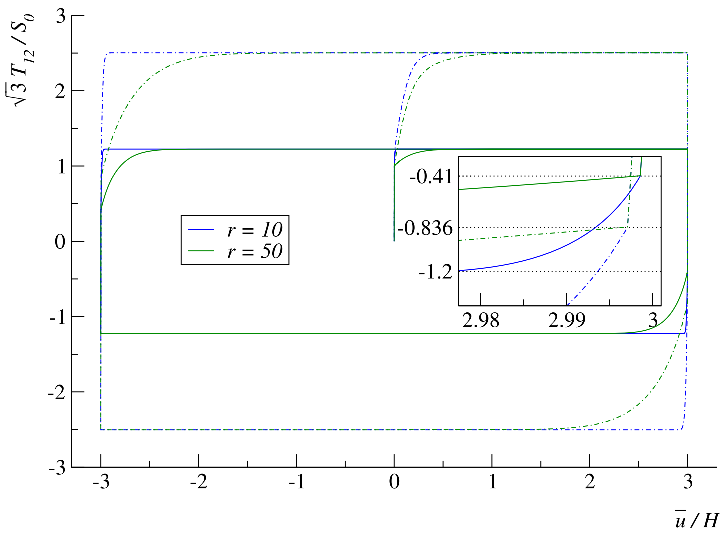

Fig. 12. Cyclic simple shear with full microhard BCs: non-dimensional Cauchy shear stress as a function of the non-dimensional applied shear displacement for $\chi = 1/3$ and $k_\Omega = 1$. Continuous and dashed lines refer to perfect plasticity and to the saturating isotropic hardening in Eq. (77), respectively.

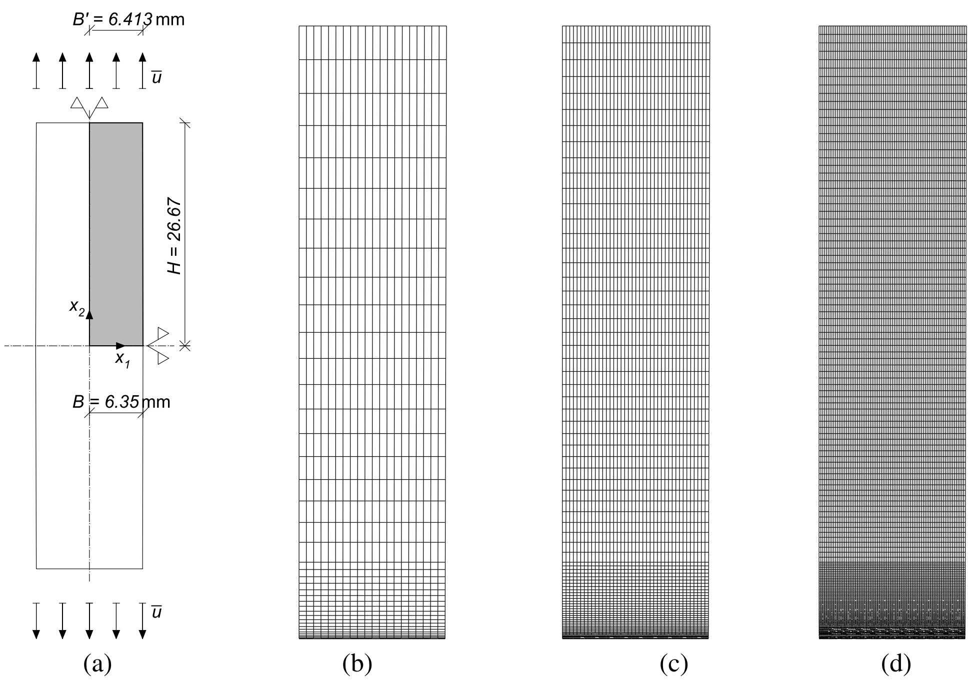

Fig. 13. Necking of a plane-strain bar: geometry (a) and three different FE meshes (b,c,d).

The values of the shear and bulk elastic moduli are

$$\mu = 79.845\,\text{GPa}, \quad k = 163.49\,\text{GPa},$$

whereas, with reference to Eq. (24), the isotropic hardening law has been selected as

$$S(\bar{\varepsilon}_p) = S_0 + S_h \bar{\varepsilon}_p^{b_h}\,.$$

Although this hardening law has a mathematical form different from that adopted in previous studies (see, e.g., de Souza Neto et al. (2008)), the material parameters

$$S_0 = 450.\,\text{MPa}\,, \quad S_h = 400.\,\text{MPa}\,, \quad b_h = 0.267$$

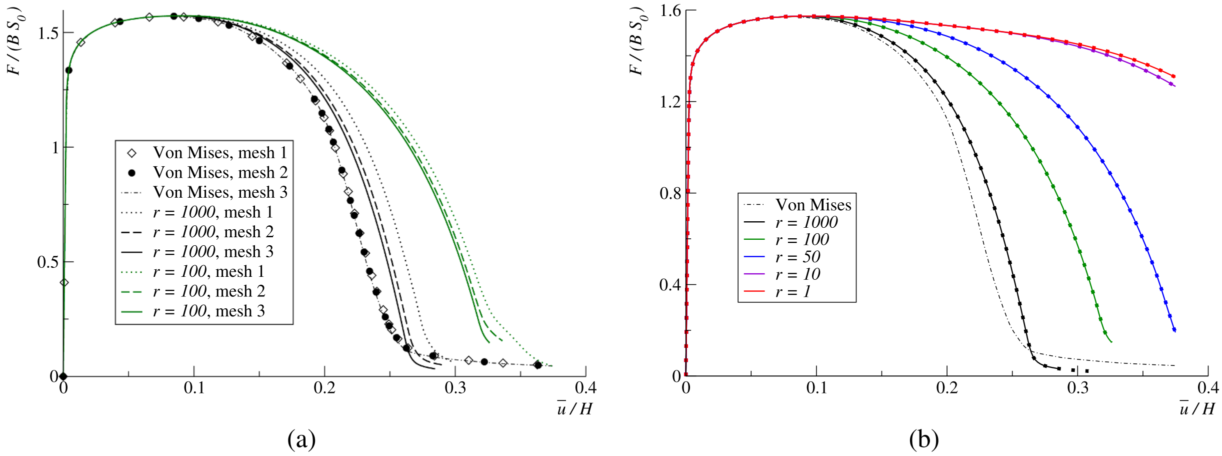

Fig. 14. Non-dimensional tensile force per unit depth vs non-dimensional applied displacement in the necking of a plane-strain bar: convergence study for the B_e model (a); response for the B_e and LN models for different values of r (b). In (b), continuous and dotted curves refer to the B_e and the LN, respectively.

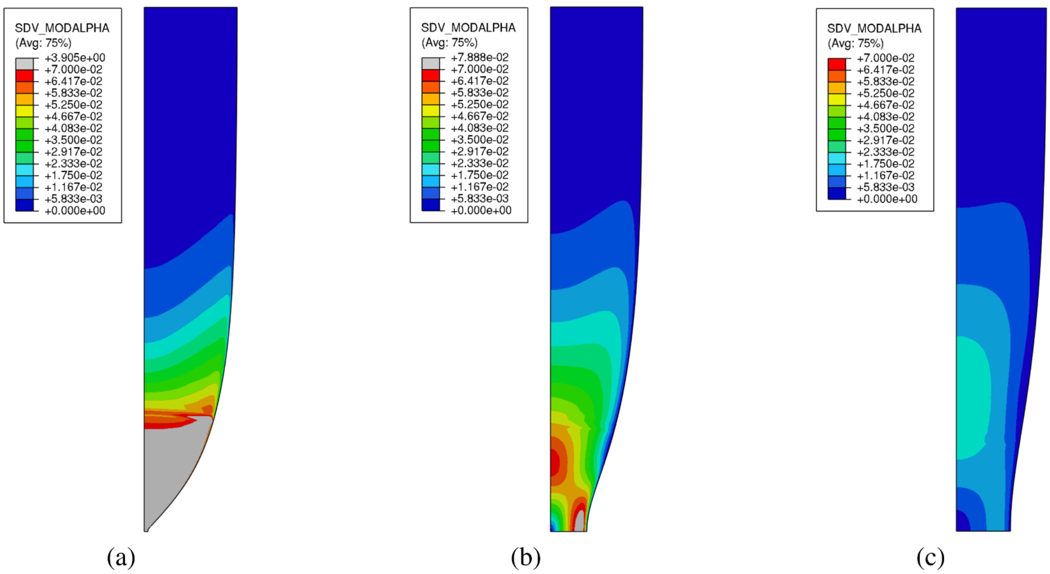

Fig. 15. Deformed shape and modulus of Nye-Kröner-like tensor for the B_e model at $\bar{u}/H = 0.2625$ at different bar sizes: $r = 1000$ (a), $r = 100$ (b), $r = 50$ (c). The unit of $|\boldsymbol{\alpha}|$ is 1/mm.

allows the two hardening forms to provide similar results in the deformation range of interest. The material parameter governing the dissipation due to the plastic spin rate is set as

$$\chi = 2/3\,.$$

Here, the size of the sample is still provided by the ratio in Eq. (66), where, however, H now denotes half of the bar length (see Fig. 13). The ratios

$$r = H/\ell = 1,\ 10,\ 50,\ 100,\ 1000$$

have been considered in order to discuss the results, which have been obtained by using both the B_e and the LN models.

The results are compared with those obtained by using conventional finite-deformation von Mises plasticity as available in the FE code Abaqus/Simulia. In this case, 8-noded quadratic FEs with reduced integration have been employed (i.e. CPE8R in the Abaqus library). Due to symmetry conditions, only the upper-right part of the domain is discretized.

The value of k_Ω in the evolution Eq. (2) for the Nye-Kröner-like tensor has been set equal to 0. Importantly, it has been checked that, for the case $r = 50$, setting $k_\Omega = 1$ yields the same results not only in terms of the force-displacement curve, but also in terms of the contour of the modulus of $(\operatorname{curl}\boldsymbol{\zeta})'$.

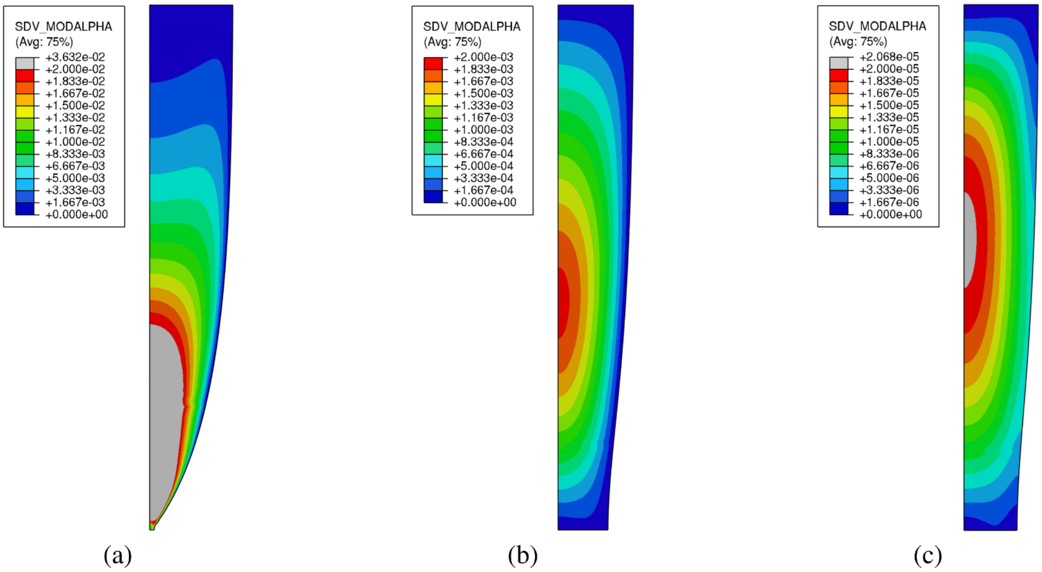

Fig. 16. Deformed shape and modulus of Nye-Kröner-like tensor at the end of the analysis, i.e. $\bar{u}/H = 0.375$, at different bar sizes: $r = 50$ (a), $r = 10$ (b), $r = 1$ (c). The unit of $|\boldsymbol{\alpha}|$ is 1/mm. Note that the scales of the contours differ of orders of magnitude.

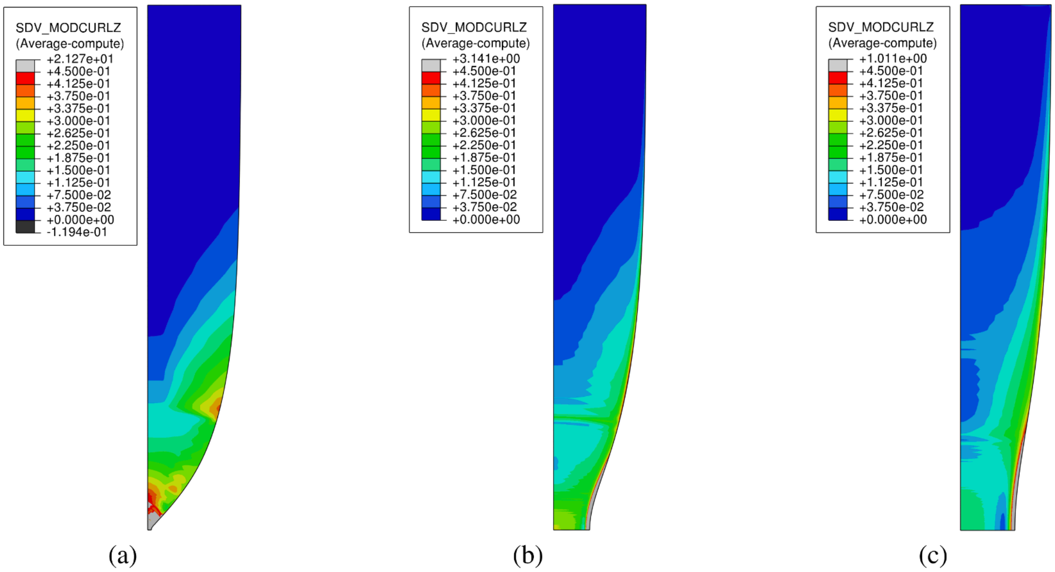

Fig. 17. Deformed shape and modulus of $(\mathrm{curl}\boldsymbol{\zeta})'$ for the B_e model at $\bar{u}/H = 0.2625$ at different bar sizes: $r = 1000$ (a), $r = 100$ (b), $r = 50$ (c). The unit of $|(\mathrm{curl}\boldsymbol{\zeta})'|$ is GPa.

Fig. 13(b–d) displays the three different FE meshes employed in this study, having, respectively, 800, 3200, and 12,800 FEs, with finer meshes including all the nodes of coarser meshes. All meshes are characterized by a discretization bias, such that the density of degrees of freedom increases towards the center of the bar, where localization is expected to occur.

Fig. 14 reports the force-displacement responses, where F denotes the tensile force per unit depth, which is computed by summing up the reaction forces at the top edge of the FE model. As shown in Fig. 14(a), a very fine mesh, specifically that displayed in Fig. 13(d), is required in order to approach mesh-converged response with the proposed $H(\mathrm{curl})$ formulation. This is because higher-order strain gradient plasticity introduces stresses associated with plastic flow gradients, here, specifically, through the Nye-Kröner-like tensor $\boldsymbol{\alpha}$. During necking, the spatial variations of $\boldsymbol{\alpha}$ become highly localized, so that the FE discretization must be fine enough to properly resolve these fields. Conventional plasticity is therefore much less sensitive to mesh refinement in this benchmark. Of course, the main result that can be deduced from Fig. 14 is that smaller the bar, less pronounced the softening behavior.

Fig. 14(b) shows that, as for the simple shear benchmark problem of Section 4.1, the B_e and LN models provide almost identical results. More interestingly, it is observed that even for the largest bar considered, corresponding to $r = 1000$, the response predicted

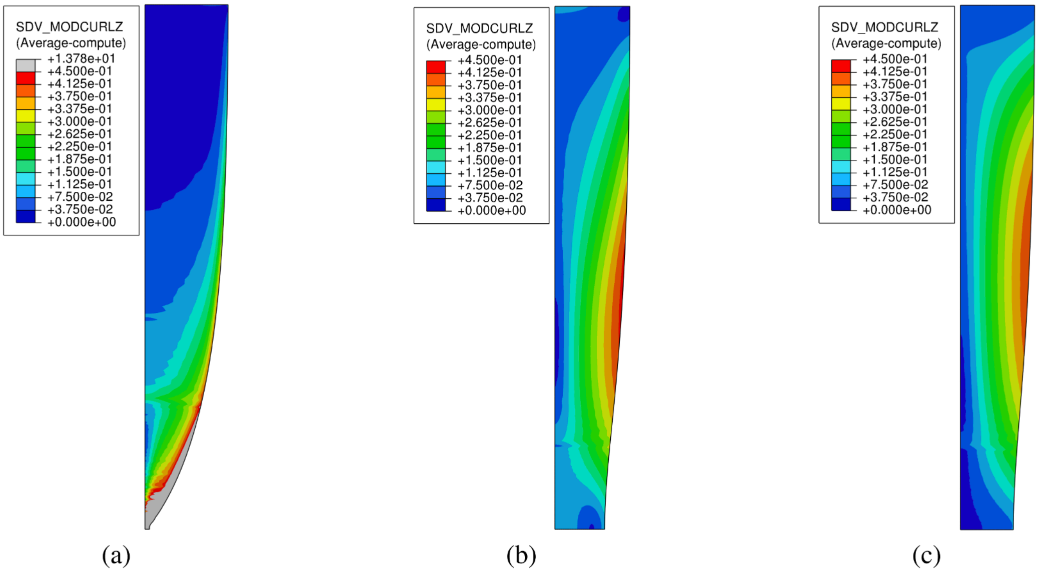

Fig. 18. Deformed shape and modulus of $(\mathrm{curl}\boldsymbol{\zeta})'$ for the B_e model at the end of the analysis, i.e. $\bar{u}/H = 0.375$, at different bar sizes: $r = 50$ (a), $r = 10$ (b), $r = 1$ (c). The unit of $|(\mathrm{curl}\boldsymbol{\zeta})'|$ is GPa.

by the $H(\mathrm{curl})$ formulation remains noticeably different from that obtained with conventional plasticity. In fact, due to large deformations, plastic flow localizes within a progressively shrinking region, where large gradients of the plastic distortion develop. As a consequence, $\boldsymbol{\alpha}$ may attain large values inside the localization zone, maintaining a non-negligible contribution of the defect stress even when H/ℓ is very large. Therefore, increasing r over 1000 would require an even much finer mesh to correctly capture the necking response.

Delving into more details, Figs. 15 and 16 show the contour of the modulus of the Nye-Kröner-like tensor, $|\boldsymbol{\alpha}|$, at two different loading levels of the analysis, in Fig. 15 at 70% of the maximum applied displacement, in Fig. 16 at the end of the analysis. Note that the larger r, the more difficult it is to apply a large displacement. Indeed, the results are provided for different bar sizes. These results clearly show that, as expected, small bars develop small $|\boldsymbol{\alpha}|$. However, it is interesting to observe that the bar region experiencing larger $|\boldsymbol{\alpha}|$ strongly depends on the bar size. By decreasing the bar size, this region turns out to be located farther from the necking zone. In fact, the significant values of the gradients of the displacement field and of $\boldsymbol{\alpha}$ are in general attained in different regions of the bar, especially at the onset of necking. Figs. 15(c) and 16(a), both referring to $r = 50$, illustrate a trend which is quite general: the bar region with larger $\boldsymbol{\alpha}$ moves down toward the center of the bar as necking progresses. Since, for a given applied displacement, localization is less pronounced for small values of r, the smaller the bar, the farther the region with large $\boldsymbol{\alpha}$ from the bar center.

Additionally, Figs. 17 and 18 show the contour of the modulus of $(\mathrm{curl}\boldsymbol{\zeta})'$, which is actually computed as $|\mathbf{M} - \mathbf{S}|$, under the assumed convergence for the higher-order balance Eq. (14). Note that the contour is cut at the value S_0. From these figures, it is very interesting to observe that the largest bar experiences the largest peak of $|(\mathrm{curl}\boldsymbol{\zeta})'|$, which is related to the obvious fact that the smaller the bar, the more hampered the plastic strain gradient.

The not-so-obvious result is that, in this benchmark, increasing r allows $|\boldsymbol{\alpha}|$ to grow so rapidly inside the localization region that this growth overcompensates the scaling factor $r^2 = (H/\ell)^2$, which is inversely proportional to the magnitude of the defect stress. As a consequence, $(\mathrm{curl}\boldsymbol{\zeta})'$ still affects the response even for the largest value of r considered. From a slightly different perspective, increasing r leads to a much more pronounced necking zone, with a smaller "active region", whose size, if possible, should be better used instead of H to define a ratio with ℓ to evaluate the influence of $\boldsymbol{\alpha}$ on the mechanical response. It is remarked that this is a finite-deformation phenomenon that cannot be modeled within the small-strain regime.

5. Concluding remarks

This work proposes an Eulerian finite-deformation extension of the distortion gradient plasticity (DGP) of Gurtin (2004), in which the Nye–Kröner tensor $\boldsymbol{\alpha}$ is adopted as the sole primal higher-order field. On the one hand, this requires a constitutive equation for the dissipation due to the plastic spin rate. On the other hand, an $H(\mathrm{curl})$ finite element (FE) implementation is needed to ensure the correct continuity requirements for the plastic rate tensor (Panteghini and Bardella, 2018).

This investigation discusses several possibilities, within the adopted Eulerian finite-deformation framework (Rubin, 2021; Rubin and Bardella, 2023), to define the required evolution equations for $\boldsymbol{\alpha}$ and for elastic distortional deformation tensor $\bar{\mathbf{B}}_e$, and even considers possible different choices for the nonlinear measure for the deviatoric elastic strain.

A fully implicit $H(\mathrm{curl})$ FE algorithm is developed and provided for plane-strain boundary value problems. To the best of the authors' knowledge, this constitutes the first $H(\mathrm{curl})$ FE formulation of DGP for finite deformations.

The proposed DGP is here applied to two benchmark problems subjected to large deformations: the cyclic simple shear of a strip and the necking of a bar under monotonic tensile loading (Simo and Armero, 1992; de Souza Neto et al., 2008).

The cyclic simple shear is studied in detail both to validate the code and to unveil features of the proposed DGP. The verification is possible by comparison with analytical results that are obtained for small strains and rotations (Panteghini and Bardella, 2018) but that, noticeably, demonstrate to hold to a large extent also for large deformations. This assessment has required the derivation of novel analytical results for the simple shear problem.

From the results for the necking problem two main conclusions can be drawn. First, the smaller the bar, the less pronounced the structural softening characterizing the force-displacement response, which is the expected size-effect in necking. Second, increasing the bar size promotes the development of large values of $\boldsymbol{\alpha}$ within a progressively shrinking localization region. It is inferred that this behavior may be a general characteristic of boundary value problems governed by finite-deformation higher-order strain gradient plasticity.

The proposed evolution equation for $\boldsymbol{\alpha}$ yields numerical results that are free from spurious oscillations. This favorable behavior may be related to the fact that, within the present DGP framework, the plastic spin is constitutively defined even in the small-strain specialization of the theory. As a consequence, the plastic rate tensor $\mathbf{L}_p$ is fully specified, and this is consistent with the adopted evolution equation for the elastic distortional tensor $\bar{\mathbf{B}}_e$, which relies on the difference between the total velocity gradient and $\mathbf{L}_p$. This appears to contribute to the robustness of the proposed formulation.

Moreover, the analysis of the results obtained by using different forms of the spin $\boldsymbol{\Omega}$ for the evolution equation of $\boldsymbol{\alpha}$ suggests that, when large rotations are dealt with, choosing $\boldsymbol{\Omega}$ to be equal to the elastic spin rate may provide a particularly effective description of the evolution of the Nye-Kröner-like dislocation density tensor.

Although the choice of the nonlinear elastic strain measure is an important constitutive assumption that should ultimately be guided by experimental evidence, the obtained results indicate that it has a negligible influence on the response for small elastic deformations, which are typical of metals. Therefore, in this case, computational efficiency may reasonably guide this choice, offering the opportunity to avoid the spectral decomposition of the distortional deformation tensor $\bar{\mathbf{B}}_e$.

5.1. Open issues

This investigation provides several interesting open issues to address in the future.

It would be important to compare both the mechanical predictions and the computational efficiency of the proposed Eulerian $H(\mathrm{curl})$ FE model with those of a finite-deformation DGP in which the Nye-Kröner-like tensor is defined on the basis of the multiplicative decomposition of the deformation gradient, $\mathbf{F} = \mathbf{F}_e\mathbf{F}_p$. This study should also focus on the comparison with experimental measurements of the dislocation density tensor (see, e.g., Gallet et al. (2023)).

A crucial open issue concerns the prediction of the actual size effects in small-scale metal plasticity. It is known that this may require the use of more sophisticated constitutive equations than those adopted in the present study. In particular, a less-than-quadratic defect energy, possibly dependent on more than a single invariant of $\boldsymbol{\alpha}$ (Bardella and Panteghini, 2015), may be needed to capture the experimentally observed increase in yield stress with diminishing size. Hence, in order to predict a reliable cyclic behavior, this may in turn require the use of a mixed recoverable-dissipative potential (Panteghini et al., 2019; Panteghini and Bardella, 2020; Bardella, 2021).

Alternatively, or complementary, to the use of complex higher-order potentials in order to predict actual size effects in small metal components, the Eulerian finite-deformation theory involving two plasticity fields, namely a higher-order field with associated Nye-Kröner-like tensor and defect stress and a conventional plasticity field, as developed in Rubin and Bardella (2023), Panteghini et al. (2025a), seems to be worthy of further development, and it would constitute an extension of the present theory. An interesting application of the present Eulerian DGP framework would, for instance, consist of the simulation of the large-deformation bending experiments of Stölken and Evans (1998).

Another interesting option to explore consists of combining the present $H(\mathrm{curl})$ FE implementation with crystal plasticity through the micromorphic approach of Forest and co-workers (see, e.g., Mukherjee et al. (2026), and references therein), so that the present model, even if limited to phenomenological plasticity, can be used for finite-deformation strain gradient crystal plasticity while avoiding the complexity of imposing higher-order boundary conditions in crystal plasticity relying on the Nye-Kröner-like tensor (Gurtin and Needleman, 2005); such a model would constitute a strong basis to study the finite-deformation behavior of grain boundaries. Another extension of the present theory consists of the development of three-dimensional $H(\mathrm{curl})$ FEs, which represents a challenging but promising research direction.

CRediT authorship contribution statement

Andrea Panteghini: Writing – review & editing, Writing – original draft, Visualization, Validation, Software, Methodology, Investigation, Formal analysis, Data curation, Conceptualization; **Lorenzo Bardella:** Writing – review & editing, Writing – original draft, Validation, Supervision, Methodology, Investigation, Formal analysis, Conceptualization; **M.B. Rubin:** Writing – review & editing, Methodology, Investigation, Formal analysis, Conceptualization.

Declaration of competing interest

The authors declare that they have no known competing financial interests or personal relationships that could have appeared to influence the work reported in this paper.

Acknowledgments

The finite element code Abaqus/Simulia has been run at the Department of Civil, Environmental, Architectural Engineering and Mathematics, University of Brescia, Italy, under an academic license. A.P. and L.B. acknowledge the support of the Italian Ministry of Education, University, and Research (MIUR). Work done under the auspices of GNFM (Gruppo Nazionale per la Fisica Matematica) of INDAM (Istituto Nazionale di Alta Matematica Francesco Severi)

Data availability

We have provided our code as Supplementary Material

Appendix A. Discussion on alternative evolution equation for $\bar{\mathbf{B}}_e$

By following the proposal in Rubin and Bardella (2023), the evolution equation for $\bar{\mathbf{B}}_e$ can be written in the form

$$\dot{\bar{\mathbf{B}}}_e = \mathbf{L}'\bar{\mathbf{B}}_e + \bar{\mathbf{B}}_e\mathbf{L}'^T - \bar{\mathbf{A}}, \quad \bar{\mathbf{A}} = 2\left[\mathbf{D}_p - \frac{\mathbf{D}_p \cdot \bar{\mathbf{B}}_e^{-1}}{\mathrm{tr}(\bar{\mathbf{B}}_e^{-1})}\mathbf{I}\right], \tag{A.1}$$

which is an alternative to Eq. (6)

Moreover, the deviatoric part of Eq. (A.1) is given by

$$\dot{\bar{\mathbf{B}}}'_e = \mathbf{L}'\bar{\mathbf{B}}_e + \bar{\mathbf{B}}_e\mathbf{L}'^T - \frac{2}{3}(\bar{\mathbf{B}}_e \cdot \mathbf{D}')\mathbf{I} - 2\,\mathbf{D}_p\,. \tag{A.2}$$

which would substitute Eq. (7).

The B_e model. In this formulation, which is the one followed in Rubin and Bardella (2023), Eq. (28) holds, such that, from Eqs. (A.1) and (8), one obtains

$$\dot{\beta}_1 = 2\bar{\mathbf{B}}'_e \cdot \mathbf{D}' + \frac{6\,\bar{\mathbf{B}}_e^{-1} \cdot \mathbf{D}_p}{\mathrm{tr}(\bar{\mathbf{B}}_e^{-1})}\,, \tag{A.3}$$

which, by using Eq. (26), leads to Eq. (29) for $\mathbf{T}'$ and

$$\mathbf{M} = -\frac{3\mu}{J\,\mathrm{tr}(\bar{\mathbf{B}}_e^{-1})}(\bar{\mathbf{B}}_e^{-1})'\,. \tag{A.4}$$

Note that the small-deformation theory can be recovered by setting

$$\bar{\mathbf{B}}_e^{-1} = \mathbf{I} - 2\boldsymbol{\varepsilon}'_e\,, \tag{A.5}$$

with $\boldsymbol{\varepsilon}'_e$ denoting the linear elastic distortional strain, in this case equal to $\bar{\mathbf{B}}'_e/2$. Then, linearizing $\mathbf{M}$ yields $\mathbf{M} = 2\mu\boldsymbol{\varepsilon}'_e$, which is equal to the deviatoric part of the Cauchy stress, as expected (Gurtin, 2004).

The LN model. In this formulation, Eq. (30) holds.

By substituting Eq. (A.1) into Eq. (31), one obtains

$$\dot{\gamma}_1 = 2\mathbf{E}'_e \cdot \mathbf{D}' + 2\left[\frac{\mathbf{E}'_e \cdot \bar{\mathbf{B}}_e^{-1}}{\mathrm{tr}(\bar{\mathbf{B}}_e^{-1})}\bar{\mathbf{B}}_e^{-1} - \bar{\mathbf{B}}_e^{-1}\mathbf{E}'_e\right] \cdot \mathbf{D}_p\,, \tag{A.6}$$

such that Eq. (26) reduces to

$$\rho\theta\xi' = \left(\mathbf{T}' - 2\frac{\rho}{\rho_z}\frac{\partial\Psi'_{\mathrm{el}}}{\partial\gamma_1}\mathbf{E}'_e\right) \cdot \mathbf{D}' - \left\{2\frac{\rho}{\rho_z}\frac{\partial\Psi'_{\mathrm{el}}}{\partial\gamma_1}\left[\frac{\mathbf{E}'_e \cdot \bar{\mathbf{B}}_e^{-1}}{\mathrm{tr}(\bar{\mathbf{B}}_e^{-1})}\bar{\mathbf{B}}_e^{-1} - \bar{\mathbf{B}}_e^{-1}\mathbf{E}'_e\right] + \mathbf{M}\right\} \cdot \mathbf{D}_p + SV(d_p)d_p \geq 0\,, \tag{A.7}$$

which implies Eq. (32) for $\mathbf{T}'$ and

$$\mathbf{M} = \frac{2\mu}{J}\left[(\bar{\mathbf{B}}_e^{-1}\mathbf{E}'_e)' - \frac{\mathbf{E}'_e \cdot \bar{\mathbf{B}}_e^{-1}}{\mathrm{tr}(\bar{\mathbf{B}}_e^{-1})}(\bar{\mathbf{B}}_e^{-1})'\right]. \tag{A.8}$$

Note that, by using Eq. (A.5) with small $\boldsymbol{\varepsilon}'_e$, $\mathbf{M}$ specializes, as expected, to the deviatoric part of the Cauchy stress, i.e. $\mathbf{M} = 2\mu\boldsymbol{\varepsilon}'_e$, in the kinematically linear case, where $\mathbf{E}'_e = \boldsymbol{\varepsilon}'_e$.

More importantly, it is known that, in contrast with the strain in Eq. (28) and other deviatoric elastic strain measures, the logarithmic strain has the property that it does not yield out-of-plane direct plastic strain rate under planar isochoric total deformation rates in size-independent, elastically isotropic, finite-deformation elastoplasticity (see, e.g., Panteghini et al. (2025b)). However, inspection of the expression (A.8) for $\mathbf{M}$ shows that this property of Hencky's strain is ineffective in this DGP, where, even under planar isochoric total deformation rates, the form of $\mathbf{M}$ in general requires out-of-plane direct plastic strain rate to satisfy the higher-order balance law Eq. (14).

An advantage of Eq. (A.1), with respect to Eqs. (4) and (5), is that the evolution equation for $\bar{\mathbf{B}}'_e$ seems to be somehow simple, as it results

$$\bar{\mathbf{A}}' = 2\mathbf{D}'_p\,.$$

A disadvantage of Eq. (A.1) is that the forms of $\mathbf{M}$ for both the B_e model, see Eq. (A.4), and the LN model, see Eq. (A.8), do not equal $\mathbf{T}'$. However, as already noticed, the values attained by $\mathbf{M}$ reduce to those of $\mathbf{T}'$ for small elastic deformations, which is typical of metals. Moreover, it is observed that the evolution Eq. (6) for $\bar{\mathbf{B}}_e$ depends explicitly on the plastic spin rate $\mathbf{W}_p$, whereas the evolution Eq. (A.1) depends on $\mathbf{W}_p$ only indirectly.

Supplementary material

Supplementary material associated with this article can be found in the online version at 10.1016/j.jmps.2026.106769

References

Abatour, M., Forest, S., Ammar, K., Ovalle, C., Osipov, N., Quilici, S., 2023. Toward robust scalar-based gradient plasticity modeling and simulation at finite deformations. Acta Mech. 234 (3), 911–958. https://doi.org/10.1007/s00707-022-03411-3

Acharya, A., Zhang, X., 2015. From dislocation motion to an additive velocity gradient decomposition, and some simple models of dislocation dynamics. Chin. Ann. Math. Ser. B 36 (5), 645–658. https://doi.org/10.1007/s11401-015-0970-0

Arora, R., Zhang, X., Acharya, A., 2020. Finite element approximation of finite deformation dislocation mechanics. Comput. Method. Appl. M. 367, 113076. https://doi.org/10.1016/j.cma.2020.113076

Arsenlis, A., Parks, D.M., 1999. Crystallographic aspects of geometrically-necessary and statistically-stored dislocation density. Acta Mater. 47 (5), 1597–1611. https://doi.org/10.1016/S1359-6454(99)00020-8

Asaro, R.J., Rice, J.R., 1977. Strain localization in ductile single crystals. J. Mech. Phys. Solids 25 (5), 309–338. https://doi.org/10.1016/0022-5096(77)90001-1

Ashby, M.F., 1970. The deformation of plastically non-homogeneous materials. Philos. Mag. 21, 399–424. https://doi.org/10.1080/14786437008238426

Aslan, O., Cordero, N.M., Gaubert, A., Forest, S., 2011. Micromorphic approach to single crystal plasticity and damage. Int. J. Eng. Sci. 49 (12), 1311–1325. Special issue: Advances in generalized continuum mechanics. https://doi.org/10.1016/j.ijengsci.2011.03.008

Bardella, L., 2009. A comparison between crystal and isotropic strain gradient plasticity theories with accent on the role of the plastic spin. Eur. J. Mech. A-Solid. 28 (3), 638–646. https://doi.org/10.1016/j.euromechsol.2008.10.006

Bardella, L., 2010. Size effects in phenomenological strain gradient plasticity constitutively involving the plastic spin. Int. J. Eng. Sci. 48 (5), 550–568. https://doi.org/10.1016/j.ijengsci.2010.01.003

Bardella, L., 2021. On a mixed energetic–dissipative constitutive law for non-proportional loading, with focus on small-scale plasticity. Proc. R. Soc. A 477 (2248), 20200940. https://doi.org/10.1098/rspa.2020.0940

Bardella, L., Giacomini, A., 2008. Influence of material parameters and crystallography on the size effects describable by means of strain gradient plasticity. J. Mech. Phys. Solids 56 (9), 2906–2934. https://doi.org/10.1016/j.jmps.2008.04.001

Bardella, L., Panteghini, A., 2015. Modelling the torsion of thin metal wires by distortion gradient plasticity. J. Mech. Phys. Solids 78, 467–492. https://doi.org/10.1016/j.jmps.2015.03.003

Bardella, L., Rubin, M.B., Panteghini, A., 2025. Eulerian rates of elastic incompatibilities for crystal plasticity applied to size-dependent hardening in finite bending. Int. J. Solid. Struct. 316, 113376. Corrigendum: Int. J. Solids Struct., 321:113558, 2025, DOI: 10.1016/j.ijsolstr.2025.113558. https://doi.org/10.1016/j.ijsolstr.2025.113376

Bilby, B.A., Gardner, L.R.T., Stroh, A.N., 1957. Continuous distributions of dislocations and the theory of plasticity. In: Proceedings of the 9th International Congress of Applied Mechanics. University de Brussels 9, 35–44.

Bittencourt, E., Needleman, A., Gurtin, M.E., van der Giessen, E., 2003. A comparison of nonlocal continuum and discrete dislocation plasticity predictions. J. Mech. Phys. Solids 51, 281–310. https://doi.org/10.1016/S0022-5096(02)00081-9

Cermelli, P., Gurtin, M.E., 2001. On the characterization of geometrically necessary dislocations in finite plasticity. J. Mech. Phys. Solids 49 (7), 1539–1568.

Conti, S., Ortiz, M. 2005. Dislocation microstructures and the effective behavior of single crystals. Arch. Ration. Mech. Anal. 176, 103–147. https://doi.org/10.1007/s00205-004-0353-2

Cordero, N.M., Gaubert, A., Forest, S., Busso, E.P., Gallerneau, F., Kruch, S., 2010. Size effects in generalised continuum crystal plasticity for two-phase laminates. J. Mech. Phys. Solids 58 (11), 1963–1994. https://doi.org/10.1016/j.jmps.2010.06.012

Dassault Systèmes, 2024. ABAQUS User's & Theory Manuals — Release 6.24. Providence, RI, USA.

de Souza Neto, E.A., Peric, D., Owen, D.R.J., 2008. Computational Methods for Plasticity. John Wiley & Sons, Ltd, Chichester, UK.

Fleck, N.A., Hutchinson, J.W., 1997. Strain gradient plasticity. Adv. Appl. Mech. 33, 295–361. https://doi.org/10.1016/S0065-2156(08)70388-0

Forest, S., Guéninchault, N., 2013. Inspection of free energy functions in gradient crystal plasticity. Acta Mech. Sinica 29 (6), 763–772. https://doi.org/10.1007/s10409-013-0088-0

Fosdick, R., Royer-Carfagni, G., 2020. Hadamard's conditions of compatibility from Cesaro's line-integral representation. Int. J. Eng. Sci. 146, 103174. https://doi.org/10.1016/j.ijengsci.2019.103174

Gallet, J., Perez, M., Guillou, R., Ernould, C., Le Bourlot, C., Langlois, C., Beausir, B., Bouzy, E., Chaise, T., Cazottes, S., 2023. Experimental measurement of dislocation density in metallic materials: A quantitative comparison between measurements techniques (XRD, R-ECCI, HR-EBSD, TEM). Mater. Charact. 199, 112842. https://doi.org/10.1016/j.matchar.2023.112842

Groma, I., Csikor, F.F., Zaiser, M., 2003. Spatial correlations and higher-order gradient terms in a continuum description of dislocation dynamics. Acta Mater. 51, 1271–1281.

Groma, I., Györgyi, G., Kocsis, B., 2007. Dynamics of coarse grained dislocation densities from an effective free energy. Philos. Mag. 87 (8–9), 1185–1199.

Gurtin, M.E., 2004. A gradient theory of small-deformation isotropic plasticity that accounts for the Burgers vector and for dissipation due to plastic spin. J. Mech. Phys. Solids 52 (11), 2545–2568. https://doi.org/10.1016/j.jmps.2004.04.010

Gurtin, M.E., 2006. The Burgers vector and the flow of screw and edge dislocations in finite-deformation single-crystal plasticity. J. Mech. Phys. Solids 54 (9), 1882–1898. https://doi.org/10.1016/j.jmps.2006.03.003

Gurtin, M.E., Needleman, A., 2005. Boundary conditions in small-deformation, single-crystal plasticity that account for the burgers vector. J. Mech. Phys. Solids 53 (1), 1–31. https://doi.org/10.1016/j.jmps.2004.06.006

Haouala, S., Lucarini, S., LLorca, J., Segurado, J., 2020. Simulation of the hall-petch effect in FCC polycrystals by means of strain gradient crystal plasticity and FFT homogenization. J. Mech. Phys. Solids 134, 103755. https://doi.org/10.1016/j.jmps.2019.103755

Hencky, H., 1933. The elastic behavior of vulcanized rubber. J. Appl. Mech.-T ASME 1 (2), 45–48. https://doi.org/10.1115/1.4012174

Jin, J.-M., 2014. The Finite Element Method in Electromagnetics. John Wiley & Sons, Inc., Hoboken, New Jersey. Third edition.

Jog, C.S., 2008. The explicit determination of the logarithm of a tensor and its derivatives. J. Elast. 93, 141–148. https://doi.org/10.1007/s10659-008-9169-x

Kaiser, T., Menzel, A., 2019. An incompatibility tensor-based gradient plasticity formulation — Theory and numerics. Comput. Method. Appl. M. 345, 671–700. https://doi.org/10.1016/j.cma.2018.11.013

Kröner, E., 1959. General continuum theory of dislocations and intrinsic stresses. Arch. Ration. Mech. Anal. 4, 273–334. https://doi.org/10.1007/BF00281393

Kröner, E., 1962. Dislocations and continuum mechanics. Appl. Mech. Rev. 15, 599–606.

Lagioia, R., Panteghini, A., Puzrin, A.M., 2014. The I_3 generalization of the Galileo-Rankine tension criterion. Proc. R. Soc. A 470 (2172), 20140568. https://doi.org/10.1098/rspa.2014.0568

Latorre, M., Montáns, F.J., 2014. On the interpretation of the logarithmic strain tensor in an arbitrary system of representation. Int. J. Solid. Struct. 51 (7), 1507–1515. https://doi.org/10.1016/j.ijsolstr.2013.12.041

Lee, E.H., 1969. Elastic-plastic deformation at finite strains. J. Appl. Mech.-T ASME 36, 1–6. https://doi.org/10.1115/1.3564580

Liu, D., He, Y., Dunstan, D.J., Zhang, B., Gan, Z., Hu, P., Ding, H., 2013. Anomalous plasticity in cyclic torsion of micron scale metallic wires. Phys. Rev. Lett. 110, 244301. https://doi.org/10.1103/PhysRevLett.110.244301

Mesarovic, S.D., Forest, S., Jaric, J.P., 2015. Size-dependent energy in crystal plasticity and continuum dislocation models. Proc. R. Soc. A 471, 20140868.

Mu, Y., Zhang, X., Hutchinson, J.W., Meng, W.J., 2016. Dependence of confined plastic flow of polycrystalline Cu thin films on microstructure. MRS Commun. 6 (3), 289–294. https://doi.org/10.1557/mrc.2016.20

Mukherjee, A., Jebahi, M., Abatour, M., Forest, S., 2026. Quantitative prediction of size effects using an advanced micromorphic approach. Mech. Mater. 218, 105679. https://doi.org/10.1016/j.mechmat.2026.105679

Nédélec, J.C., 1980. Mixed finite elements in $\mathfrak{R}^3$. Numer. Math. 35 (3), 315–341. https://doi.org/10.1007/BF01396415

Nye, J.F., 1953. Some geometrical relations in dislocated crystals. Acta Metall. 1, 153–162. https://doi.org/10.1016/0001-6160(53)90054-6

Ohno, N., Okumura, D., 2007. Higher-order stress and grain size effects due to self-energy of geometrically necessary dislocations. J. Mech. Phys. Solids 55, 1879–1898. https://doi.org/10.1016/j.jmps.2007.02.007

Panteghini, A., 2024. A simple spectral representation of a second-order symmetric tensor and its variation. Eur. J. Mech. - A/Solid. 104, 105208. https://doi.org/10.1016/j.euromechsol.2023.105208

Panteghini, A., Bardella, L., 2016. On the finite element implementation of higher-order gradient plasticity, with focus on theories based on plastic distortion incompatibility. Comput. Method. Appl. M. 310, 840–865. https://doi.org/10.1016/j.cma.2016.07.045

Panteghini, A., Bardella, L., 2018. On the role of higher-order conditions in distortion gradient plasticity. J. Mech. Phys. Solids 118, 293–321. https://doi.org/10.1016/j.jmps.2018.05.019

Panteghini, A., Bardella, L., 2020. Modelling the cyclic torsion of polycrystalline micron-sized copper wires by distortion gradient plasticity. Philos. Mag. 100 (18), 2352–2364. https://doi.org/10.1080/14786435.2020.1766144

Panteghini, A., Bardella, L., Niordson, C.F., 2019. A potential for higher-order phenomenological strain gradient plasticity to predict reliable response under non-proportional loading. Proc. R. Soc. A 475 (2229), 20190258. https://doi.org/10.1098/rspa.2019.0258

Panteghini, A., Bardella, L., Rubin, M.B., 2025a. Modeling yield stress scaling and cyclic response using a size-dependent theory with two plasticity rate fields. J. Mech. Phys. Solids 194, 105930. https://doi.org/10.1016/j.jmps.2024.105930

Panteghini, A., Rubin, M.B., Bardella, L., 2025b. Assessment of isotropic large-deformation elastoplasticity models with lode angle dependence. Comput. Method. Appl. M. 446, 118275. https://doi.org/10.1016/j.cma.2025.118275

Poh, L.H., Peerlings, R.H.J., 2016. The plastic rotation effect in an isotropic gradient plasticity model for applications at the meso scale. Int. J. Solid. Struct. 78–79, 57–69. https://doi.org/10.1016/j.ijsolstr.2015.09.017

Rognes, M.E., Kirby, R.C., Logg, A., 2010. Efficient assembly of H(div) and H(curl) conforming finite elements. SIAM J. Sci. Comput. 31 (6), 4130–4151. https://doi.org/10.1137/08073901X

Rubin, M.B., 1994. Plasticity theory formulated in terms of physically based microstructural variables – Part I. Theory. Int. J. Solid. Struct. 31, 2615–2634.

Rubin, M.B., 2012. Removal of unphysical arbitrariness in constitutive equations for elastically anisotropic nonlinear elastic–viscoplastic solids. Int. J. Eng. Sci. 53, 38–45. https://doi.org/10.1016/j.ijengsci.2011.12.008

Rubin, M.B., 2021. Continuum Mechanics with Eulerian Formulations of Constitutive Equations. Springer Nature.

Rubin, M.B., Attia, A.V., 1996. Calculation of hyperelastic response of finitely deformed elastic-viscoplastic materials. Int. J. Num. Meth. Eng. 39, 309–320. 10.1002/(SICI)1097-0207(19960130)39:2<309::AID-NME858>3.0.CO;2-B

Rubin, M.B., Bardella, L., 2023. An Eulerian thermodynamical formulation of size-dependent plasticity. J. Mech. Phys. Solids 170, 105122. https://doi.org/10.1016/j.jmps.2022.105122

Rubin, M.B., Bardella, L., 2024. Eulerian rates of elastic incompatibilities applied to size-dependent hardening in finite torsion. J. Mech. Phys. Solids 193, 105905. https://doi.org/10.1016/j.jmps.2024.105905

Simo, J.C., 1992. Algorithms for static and dynamic multiplicative plasticity that preserve the classical return mapping schemes of the infinitesimal theory. Comput. Method. Appl. M. 99 (1), 61–112. https://doi.org/10.1016/0045-7825(92)90123-2

Simo, J.C., Armero, F., 1992. Geometrically non-linear enhanced strain mixed methods and the method of incompatible modes. Int. J. Num. Meth. Eng. 33 (7), 1413–1449. https://doi.org/10.1002/nme.1620330705

Steinmann, P., 1996. Views on multiplicative elastoplasticity and the continuum theory of dislocations. Int. J. Eng. Sci. 34 (15), 1717–1735. https://doi.org/10.1016/S0020-7225(96)00062-6

Stölken, J.S., Evans, A.G., 1998. A microbend test method for measuring the plasticity length scale. Acta Mater. 46, 5109–5115. https://doi.org/10.1016/S1359-6454(98)00153-0

Wieners, C., Wohlmuth, B., 2011. A primal-dual finite element approximation for a nonlocal model in plasticity. SIAM J. Numer. Anal. 49, 692–710. https://doi.org/10.1137/100789397

Willis, J.R., 1967. Second-order effects of dislocations in anisotropic crystals. Int. J. Eng. Sci. 5 (2), 171–190. https://doi.org/10.1016/0020-7225(67)90003-1

Wulfinghoff, S., Forest, S., Böhlke, T., 2015. Strain gradient plasticity modelling of the cyclic behaviour of laminate microstructures. J. Mech. Phys. Solids 79, 1–20. https://doi.org/10.1016/j.jmps.2015.02.008

Zecevic, M., Lebensohn, R.A., Capolungo, L., 2023. Non-local large-strain FFT-based formulation and its application to interface-dominated plasticity of nano-metallic laminates. J. Mech. Phys. Solids 173, 105187. https://doi.org/10.1016/j.jmps.2022.105187